

BARI-TH/365-99

# Three-flavor MSW solutions of the solar neutrino problem

G. L. Fogli <sup>a</sup>, E. Lisi <sup>a</sup>, D. Montanino <sup>b</sup>, and A. Palazzo <sup>a</sup>

<sup>a</sup> *Dipartimento di Fisica and Sezione INFN di Bari,  
Via Amendola 173, I-70126 Bari, Italy*

<sup>b</sup> *Dipartimento di Scienza dei Materiali dell'Università di Lecce,  
Via Arnesano, Collegio Fiorini, I-73100 Lecce, Italy*

## Abstract

We perform an updated phenomenological analysis of the Mikheyev-Smirnov-Wolfenstein (MSW) solutions of the solar neutrino problem, assuming oscillations between two and three neutrino families. The analysis includes the total rates of the Homestake, SAGE, GALLEX, Kamiokande and Super-Kamiokande experiments, as well as the day-night asymmetry and the 18-bin energy spectrum of Super-Kamiokande. Solutions are found at several values of the  $\theta_{13}$  mixing angle. Among the most interesting features, we find that solar neutrino data alone put the constraint  $\theta_{13} \lesssim 55^\circ - 59^\circ$  at 95% C.L., and that a fraction of the MSW solutions extends at and beyond maximal ( $\nu_1, \nu_2$ ) mixing ( $\theta_{12} \geq \pi/4$ ), especially if the neutrino square mass splitting is in its lower range ( $m_2^2 - m_1^2 \sim 10^{-7}$  eV<sup>2</sup>) and if  $\theta_{13}$  is nonzero. In particular, bimaximal (or nearly bimaximal) mixing is possible for atmospheric and MSW solar neutrino oscillations within the stringent reactor bounds on  $\theta_{13}$ .

PACS number(s): 26.65.+t, 13.15.+g, 14.60.Pq, 91.35.-x

Typeset using REVTEX

## I. INTRODUCTION

It is widely recognized that the combined sources of evidence for neutrino flavor transitions coming from the solar neutrino problem [1] and from the atmospheric neutrino anomaly [2] demand an approach in terms of three-flavor oscillations among massive neutrinos ( $\nu_1, \nu_2, \nu_3$ ) [3]. The three-flavor  $\nu$  parameter space is then spanned by six variables:

$$\delta m^2 = m_2^2 - m_1^2 , \quad (1a)$$

$$m^2 = m_3^2 - m_2^2 , \quad (1b)$$

$$\omega = \theta_{12} \in [0, \pi/2] , \quad (1c)$$

$$\phi = \theta_{13} \in [0, \pi/2] , \quad (1d)$$

$$\psi = \theta_{23} \in [0, \pi/2] , \quad (1e)$$

$$\delta = \text{CP violation phase} , \quad (1f)$$

where the  $\theta_{ij}$  rotations are conventionally ordered as for the quark mixing matrix [4].

In the phenomenologically interesting limit  $|\delta m^2| \ll |m^2|$ , the two eigenstates closest in mass ( $\nu_1, \nu_2$ ) drive solar neutrino oscillations, while the “lone” eigenstate  $\nu_3$  drives atmospheric neutrino oscillations. In such a limit (see [3,4] and refs. therein): *i*) the phase  $\delta$  becomes unobservable; *ii*) the atmospheric parameter space is spanned by  $(m^2, \psi, \phi)$ ; and *iii*) the solar neutrino parameter space is spanned by  $(\delta m^2, \omega, \phi)$ .<sup>1</sup>

Building on a previous work [5], we perform a thorough analysis of the available solar neutrino data in the  $(\delta m^2, \omega, \phi)$  variables, in the context of the Mikheyev-Smirnov-Wolfenstein (MSW) oscillation mechanism [6]. There are several motivations to revisit, update and improve the analysis in [5], the most important being the need to include the high-statistics Super-Kamiokande (SK) observations of neutrino events (total rate, [2], energy spectrum [2,7], and day-night difference [2,8]). Indeed, the few post-SK papers on three-flavor MSW oscillations we are aware of [9–11] include neither the spectrum information nor day-night variations. This contrasts with the more familiar two-family MSW analyses, which have been regularly updated with state-of-the-art global fits at different detector lifetime days; see, e.g., the SK official fits ([2,12,13] and refs. therein), as well as various analyses by independent research groups: [14] (100 days), [15] (300 days), [16] (500 days), and [17,18] (800 days).

After the work [5], there have been also other relevant experimental and theoretical improvements (implemented in the present analysis): updated measurements of the experimental (total) rates in the chlorine (Cl) [19] and Kamiokande (K) [20] experiments and in the gallium (Ga) detectors SAGE [21] and GALLEX [22]; new standard solar model (SSM) estimates for the neutrino fluxes and their uncertainties, and for the neutrino production regions in the Sun [23]; updated calculations of the  ${}^8\text{B}$  neutrino spectrum [24], of the  $\nu_{e,\mu}$  scattering cross section on electrons [25], and of the  $\nu_e$  neutrino absorption cross section

<sup>1</sup> In the special case  $\phi = 0$ , the atmospheric and solar parameter spaces are decoupled into the two-family oscillation spaces  $(\delta m^2, \omega)$  and  $(m^2, \psi)$ .

in chlorine [24] and in gallium [26]; analytical methods to compute the (time-averaged)  $\nu_e$  survival probability in the Earth [27].

In addition, some relatively old topics, such as the role played by a possibly large *hep* neutrino flux [28,29], or by solar neutrino mixing at and beyond “maximal” values ( $\omega \geq \pi/4$ ) [5], are currently being revisited (see [30–32] and [33–35], respectively) and demand an updated discussion. In particular, the case of maximal solar neutrino mixing ( $\omega = \pi/4$ ) appears now more “natural” and interesting in light of the Super-Kamiokande results on atmospheric neutrinos, which favor maximal  $\nu_\mu \leftrightarrow \nu_\tau$  mixing ( $\psi = \pi/4$ ).<sup>2</sup> Therefore, it is important to go beyond the usual analyses in terms of the solar  $\nu$  mixing parameter  $\sin^2 2\omega$  (equivalent to take  $\omega \leq \pi/4$ ), which miss a potentially interesting region of the MSW solutions at  $\omega > \pi/4$ , as we shall see later (see also [5] for earlier discussions).

Concerning the parameter  $\phi$ , we do not include *a priori* the constraints coming from the CHOOZ reactor experiment [39], which, together with the atmospheric neutrino data [2], imply that  $\sin^2 \phi \lesssim \text{few \%}$  [40,35] (the exact upper limit depending on the value of  $m^2$ , on the confidence level chosen, and on the number of degrees of freedom in the oscillation model). In fact, we think that it is instructive to study the constraints on  $\phi$  coming from solar neutrino data *alone*, as it has been done similarly for atmospheric neutrino data [40].

In any case, observable effects on the MSW solutions can be generated even by small (few %) values of  $\sin^2 \phi$ , which induce a fractional suppression in the solar neutrino survival probability  $P_{ee}$  approximately equal to  $2 \times \sin^2 \phi$ . In fact, if  $N_e$  is the electron density profile, the  $3\nu$  and  $2\nu$  expressions for  $P_{ee}$  are related by the expression

$$P_{ee}^{3\nu}(\delta m^2, \omega, \phi) = \sin^4 \phi + \cos^4 \phi \cdot P_{ee}^{2\nu}(\delta m^2, \omega) \Big|_{N_e \rightarrow \cos^2 \phi N_e}, \quad (2)$$

which, for small values of  $\phi$ , gives roughly

$$\frac{P_{ee}^{3\nu} - P_{ee}^{2\nu}}{P_{ee}^{2\nu}} \simeq -2 \sin^2 \phi. \quad (3)$$

Even within the stringent CHOOZ limits on  $\sin^2 \phi$ , such variations of  $P_{ee}$  can become as large as the uncertainties on the neutrino event rates, and thus cannot be neglected.

The above motivations warrant the present work, which is organized as follows. In Sec. II we present the theoretical and experimental ingredients of the analysis. In Sec. III we update the familiar two-family oscillation fit ( $\phi = 0$ ), and discuss in detail the features of the  $2\nu$  MSW solutions. In Sec. IV we extend the analysis to three-flavor oscillations, and discuss how the  $3\nu$  MSW solutions change for increasing values of  $\phi$ . We summarize our results in Sec. V. The details of the statistical analysis are given in the Appendix.

---

<sup>2</sup>Solar  $\nu$  MSW oscillations at  $\sin^2 2\omega = 1$  are nontrivial when Earth matter effects are included [5,33–35]. This fact was not considered in Refs. [36–38], where only matter effects in the Sun were studied.

## II. STANDARD PREDICTIONS AND EXPERIMENTAL DATA

In the present analysis, we use the so-called BP98 standard solar model [23] for the electron density in the Sun and for the input neutrino parameters ( $\nu_e$  fluxes, spectra, and production regions), and compare the predictions to the experimental data for the following observables: total neutrino event rates, SK energy spectrum, and SK day-night asymmetry.

Table I shows the latest results (and standard expectations) for the total neutrino event rates measured at Homestake [19], Kamiokande [20], SAGE [21], GALLEX [22], and Super-Kamiokande (825 live days) [2,12,13]. Since the SAGE and GALLEX detectors measure exactly the same quantity (up to a negligible difference in the detector latitude), their results are combined in a single (Ga) rate of  $72.5 \pm 5.6$  SNU. On the other hand, the Kamiokande and Super-Kamiokande data are treated separately (rather than combined in a single datum), since the two experiments, although based on the same  $\nu$ - $e$  scattering detection technique, have rather different energy thresholds and resolution functions.<sup>3</sup>

The SK electron recoil energy spectrum and its statistical and systematic uncertainties (825 lifetime day,  $E_e > 5.5$  MeV) are graphically reduced from the 18-bin histograms shown by SK members in recent Summer '99 conferences [2,12,13]. The corresponding numerical values have been already reported in detail in Ref. [17] and are not repeated here. Our theoretical calculation of the binned spectrum properly takes into account energy threshold and resolution effects (see, e.g., the Appendix of Ref. [41]). Standard  ${}^8\text{B}$  [24] and *hep* [23] neutrino spectra and fluxes are used, unless otherwise noted. Concerning the SK day-night asymmetry of the event rates, we use the latest measurement [13]:

$$2 \frac{N - D}{N + D} = 0.065 \pm 0.031 \pm 0.013 . \quad (4)$$

In the presence of  $2\nu$  or  $3\nu$  oscillations, the MSW effect in the Sun is computed as described in Ref. [5]. The additional Earth matter effects are treated as in Ref. [27]. The  $\chi^2$  analysis of the theoretical and experimental uncertainties basically follows the approach developed in [42], with the necessary updates to take into account the BP98 SSM predictions and the energy spectrum information. Technical details about error estimates are given in the Appendix.

We conclude this section by comparing the standard (no oscillation) predictions with the experimental data for the Cl, Ga, and SK total rates. Figure 1 shows the 99% C.L. error ellipses for data and expectations in the planes charted by the (Cl, Ga), (SK, Ga), and (SK, Cl) total rates. The distance between observations and standard predictions makes the solar neutrino problem(s) evident. At present, such information is the main evidence for solar neutrino physics beyond the standard electroweak model; however, since the theoretical

<sup>3</sup>The inclusion of the Kamiokande rate is currently not decisive in shaping the MSW solutions, the SK rate being much more accurately measured. However, its addition to the Cl, Ga, and SK rates avoids a situation of “zero degrees of freedom” in the  $\chi^2$  fit to the total rates for the  $3\nu$  MSW case [three data (Cl, Ga, SK) minus three free parameters ( $\delta m^2, \omega, \phi$ )]. In such a situation, the value of  $\chi^2_{\min}$  would not have a well-defined likelihood.

errors are dominant—as far as total rates are concerned—no substantial improvements can be expected by a reduction of the experimental errors. Conversely, decisive information is expected from the SK spectrum and day-night asymmetry, but no convincing deviation has emerged from such data yet. Therefore, it is not surprising that, in oscillation fits, the total rates mainly determine *allowed* regions, while the SK spectrum and day-night asymmetry determine *excluded* regions.

### III. TWO-FLAVOR MSW OSCILLATIONS

Figure 2 shows the results of our  $2\nu$  MSW analysis of the data discussed in the previous section, shown as confidence level contours in the  $(\delta m^2, \sin^2 2\omega / \cos 2\omega)$  plane. The choice of the variable  $\sin^2 2\omega / \cos 2\omega$ , rather than the usual  $\sin^2 2\omega$ , allows an expanded view of the large mixing region. In each of the six panels, we determine the absolute minimum of the  $\chi^2$  and then plot the iso- $\chi^2$  contours at  $\chi^2 - \chi_{\min}^2 = 4.61, 5.99$ , and  $9.21$ , corresponding to  $90\%$ ,  $95\%$ , and  $99\%$  C.L. for two degrees of freedom (the oscillation parameters). In fits including the total rates, there is a global  $\chi^2$  minimum and two local mimima; such minima, and the surrounding favored regions, are usually indicated as MSW solutions at small mixing angle (SMA), large mixing angle (LMA), and low  $\delta m^2$  (LOW). Additional information on such solutions is reported in Tab. II.

Concerning the statistical interpretation of the  $\chi^2$  values, a remark is in order. One can attach confidence levels to  $\chi^2$  values in two different ways, depending on the choice between *hypotheses tests* and *parameter estimation* [43]. If one is interested in testing the goodness of the MSW hypothesis *a priori*, then one should compare the absolute  $\chi_{\min}^2$  with a number of degrees of freedom ( $N_{\text{DF}}$ ) calculated as number of data minus number of free parameters. The corresponding probability  $P$  is given in the last column of Tab. II where, for completeness,  $P$  is reported also for the other two local minima and for the no oscillation case. If the MSW hypothesis is accepted, then the MSW parameter estimation involves only  $\chi^2$  differences with respect to the global minimum, and the appropriate value of  $N_{\text{DF}}$  to use is the number of free parameters in the model ( $N_{\text{DF}} = 2$ ), as anticipated for Fig. 2.

The first panel of Fig. 2 refers to the fit to the total rates only. The three  $\chi^2$  minima are indicated by dots. The absolute minimum is reached within the SMA solution ( $\chi_{\min}^2 = 1.08$ ), which represents a very good fit to the data. The LMA solution is also acceptable, while the LOW solution gives a marginal fit (see also the upper three rows of Tab. II). The SK data on the day-night asymmetry (second panel) and energy spectrum (third panel) exclude large regions in the mass-mixing parameter space; but are unable to (dis)prove any of the three solutions, which in fact are present also in the global fit to all data (fifth panel; see also the middle three rows of Tab. II).

The spectrum information is somewhat sensitive to the (uncertain) value of the *hep* neutrino flux; for instance, an enhancement by a factor 20 helps to fit the high-energy part of the SK spectrum [30], and thus it produces a reduction of the excluded regions in the mass-mixing plane (fourth panel in Fig. 2), and a corresponding slight enlargement of the

globally allowed regions (sixth panel; see also the lower three rows of Tab. II).<sup>4</sup>

From the results of Fig. 2 and of Tab. II, it appears that the inclusion of the day-night and spectral information can significantly change the C.L.’s associated to each of three solutions SMA, LMA, and LOW. In order to understand better the role of difference pieces of data, we show in Fig. 3 the comparison between data and predictions for the  $\chi^2_{\min}$  point of the total rate fit (SMA solution at best fit, first row of Tab. II), in the same coordinates as in Fig. 1. Analogously, Figs. 4 and 5 show the analogous comparison for the LMA and LOW solutions (second and third row of Tab. II). Figure 6 shows the spectral information for the three local minima in the global fit to all data with standard *hep* flux (upper panel) and with enhanced ( $20\times$ ) *hep* flux (lower panel).

From Figs. 3–5 it appears (as far as total rates are concerned) that the SMA solution represents a very good fit to the SK, Ga, and Cl data, that the LMA solution underestimates slightly the Ga and SK data, and that the LOW solution underestimates the Ga rate and overestimates the Cl rate. This explains the ordering in the likelihood of such solutions in Tab. II:  $P(\text{SMA}) > P(\text{LMA}) > P(\text{LOW})$ . On the other hand, Figure 6 shows that the bulk of the SK observed spectrum is basically consistent with a flat shape (except for the two highest-energy, low-statistics bins), and therefore tends to favor the LMA and LOW solutions, rather than the steadily increasing spectrum predicted by the SMA solution. This tendency is slightly enhanced in the case of large *hep* neutrino flux (lower panel of Fig. 6) since in this case the LMA and LOW solutions can fit somewhat better the spectrum endpoint. In other words, the inclusion of the spectrum in the global analysis tends to compensate the different likelihoods of the LMA and LOW solutions with respect to the SMA solution. Moreover, the slight excess of observed nighttime events [Eq. (4)] adds extra likelihood to the LMA solution, so that in the global fit one has  $P(\text{SMA}) \sim P(\text{LMA}) > P(\text{LOW})$  (see Tab. II), with the LMA solution even more likely than the SMA solution in the case of large *hep* flux.

From the previous discussion, the following situation emerges for the three MSW solutions SMA, LMA, and LOW. None of them can be excluded at 99% C.L. by the present experimental data. Different pieces of data give indications that are not as consistent as it would be desirable: the total rate information favors the SMA solution, the spectral data favor the LMA and LOW solutions, and the day-night data favor the LMA solution. In a global fits, the three solutions have comparable likelihoods. Although such solutions are subject to change shape and likelihood as more accurate experimental data become available, no dramatic improvement can be really expected in their selection, unless: 1) the theoretical uncertainties on the total rates are reduced to the size of the corresponding experimental uncertainties; 2) the total errors associated to the SK spectrum and day-night measurement are significantly reduced (by, say, a factor  $\sim 2$ ); or 3) decisive results are found in new solar neutrino experiments such as the Sudbury Neutrino Observatory (SNO) [18,44,45], the Gal-

<sup>4</sup>The SK Collaboration [12] derives a preliminary upper limit of  $\sim 15$  to the *hep*/SSM flux ratio (in the absence of oscillations). This limit is weakened to  $\lesssim 30$  in the presence of an oscillation effect of  $\sim 50\%$ . Therefore, we can assume  $20\times$  *hep* as a relevant, representative case of large *hep* flux.

lum Neutrino Observatory [46,47], BOREXINO [48,47], and KamLand [49]. Any of these conditions require a time scale of a few years at least; the same time scale should then be expected in order to (patiently) single out one of the three MSW solutions (SMA, LMA, or LOW).

Another aspect of the LMA and LOW solutions emerging from Fig. 2 is their extension to large values of the mixing angle ( $\sin^2 2\omega \rightarrow 1$ ), which are often assumed to be realized only through the vacuum oscillation solutions. Since the possibility of nearly maximal ( $\nu_1, \nu_2$ ) mixing for solar neutrinos has gained momentum after the SK evidence for maximal ( $\nu_\mu, \nu_\tau$ ) mixing ( $\sin^2 2\psi \sim 1$ ), it is interesting to study it in detail by dropping the usual “ $2\omega$ ” variable and by exploring the full range  $\omega \in [0, \pi/2]$ , as it was done earlier in [5]. The subcase  $\omega = \pi/4$  will receive special attention in the next section.

#### IV. THREE-FLAVOR MSW OSCILLATIONS

As stated in Sec. I, for large values of  $m^2$  ( $\gg 10^{-4}$  eV $^2$ ) the parameter space relevant for  $3\nu$  solar neutrino oscillations is spanned by the variables  $(\delta m^2, \omega, \phi)$ . As far as  $\omega$  is taken in its full range  $[0, \pi/2]$ , one can assume  $\delta m^2 > 0$ , since the MSW physics is invariant under the substitution  $(\delta m^2, \omega) \rightarrow (-\delta m^2, \pi/2 - \omega)$  at any  $\phi$ .<sup>5</sup>

For graphical representations, we prefer to use the mixing variables  $(\tan^2 \omega, \tan^2 \phi)$  introduced in [5], which properly chart both cases of small and large mixing. The case  $\tan^2 \phi = 0$  corresponds to the familiar two-family oscillation scenario, except that now we consider also the usually neglected case  $\omega > \pi/4$  ( $\tan^2 \omega > 1$ ). For each set of observables (rates, spectrum, day-night difference, and combined data) we compute the corresponding MSW predictions and their uncertainties, identify the absolute minimum of the  $\chi^2$  function, and determine the surfaces at  $\chi^2 - \chi_{\min}^2 = 6.25, 7.82$ , and  $11.36$ , which define the volumes constraining the  $(\delta m^2, \tan^2 \omega, \tan^2 \phi)$  parameter space at 90%, 95%, and 99% C.L. Such volumes are graphically presented in  $(\delta m^2, \tan^2 \omega)$  slices for representative values of  $\tan^2 \phi$ .

Figure 7 shows the results for the fit to the total rates only. The absolute minimum ( $\chi_{\min}^2 = 0.7$ ) is reached within the SMA solution at nonzero  $\tan^2 \phi$ , as reported in the first row of Tab. III. The preference for  $\phi \neq 0$  is, however, not statistically significant, since  $\chi_{\min}^2(\phi = 0) - \chi_{\min}^2 = 1.08 - 0.70 = 0.38$  only. The qualitative behavior of the  $3\nu$  MSW solutions in Fig. 7 is unchanged with respect to the earlier analysis in [5]: for increasing  $\tan^2 \phi$ , the LOW solution moves to slightly larger values of  $\tan^2 \omega$  and then disappears, while the SMA and LMA regions tend to merge in a single, broad solution which slowly disappears at large values of  $\phi$ . In general, the MSW allowed region(s) become less structured for increasing  $\phi$ , due to the decreasing energy dependence of the  $\nu_e$  survival probability [5]. In the first panel of Fig. 7 it is interesting to note that both the LMA and the LOW solutions are compatible at 99% C.L. with maximal mixing ( $\tan^2 \omega = 1$ ). This compatibility persists for the LOW solution at small values of  $\tan^2 \phi$ , while it is lost for the LMA solution, which migrates towards smaller mixing angles. As for the two-family case discussed in the

---

<sup>5</sup>Only for solar neutrino oscillations in *vacuum*, the further symmetry  $\omega \rightarrow \pi/2 - \omega$  (at any  $\delta m^2$  and  $\phi \in [0, \pi/2]$ ) allows to take  $\delta m^2 > 0$  with  $\omega$  in the restricted range  $[0, \pi/4]$ .

previous section, the addition of the spectrum information (and, to a lesser extent, of the day-night asymmetry) is expected to produce significant changes in the C.L.’s associated to the MSW solutions in Fig. 7.

Figure 8 shows the region excluded by the SK day-night asymmetry, in the same representation as in Fig. 7. Such region is generally far from the allowed regions in Fig. 7, and thus the day-night asymmetry contributes only marginally to shape the MSW solutions, except at low values of  $\tan^2 \phi$ , where it cuts the lower part of the LMA solution and disfavors the rightmost part of the SMA solution. The region excluded by the SK day-night asymmetry can extend beyond maximal mixing ( $\tan^2 \omega > 1$ ), as it was observed earlier in Ref. [5] for the corresponding Kamiokande variable.

Figure 9 shows instead the regions excluded by the SK spectrum, which plays a relevant role in disfavoring the zone where the SMA and LMA solutions tend to merge (see the six middle panels of Fig. 7). In fact, for  $\delta m^2 \sim 10^{-4}$  eV $^2$  the normalized SK spectrum is predicted to have a large *negative* slope (see, e.g., [27]), contrary to the experimental results. Relatively large positive values for the spectrum slope are excluded in the left diagonal band shown in the upper panels of Fig. 9. Both positive and negative values for the spectrum slope can instead occur in the excluded region where the Earth regeneration effects are relevant [27]. For increasing  $\phi$ , the spectral information becomes less effective in disfavoring zones of the parameter space, since the energy-dependence of the electron survival probability becomes weaker. Therefore, only the strongest distortion effect (at  $\delta m^2 \sim 10^{-4}$  eV $^2$ ) survives at large  $\tan^2 \phi$ . Finally, as in the  $2\nu$  case, the excluded regions are slightly shrunk if large *hep* flux values are assumed (not shown).

Figure 10 shows the combined fit to all data, which is one of the main results of this work. As for the total rates, the minimum  $\chi^2$  (second row of Tab. III) is reached within the SMA solution and shows a very weak preference for nonzero values of  $\phi$  ( $\tan^2 \phi \simeq 0.1$ ). By comparing Fig. 10 with Fig. 7, it can be seen that the SK spectrum excludes a significant fraction of the solutions at  $\delta m^2 \sim 10^{-4}$  eV $^2$ , including the upper part of the LMA solution at small  $\phi$ , and the merging with the SMA solution at large  $\phi$ . In particular, at  $\tan^2 \phi = 0.1$  the 95% C.L. upper limit on  $\delta m^2$  drops from  $2 \times 10^{-4}$  eV $^2$  (rates only) to  $8 \times 10^{-5}$  eV $^2$  (all data). This indication tends to disfavor neutrino searches of *CP* violation effects, since such effects decrease with  $\delta m^2/m^2$  at nonzero values of  $\phi$ .

Figure 10 also shows that the inclusion of the present spectrum and day-night information, rather than helping in constraining  $\tan^2 \phi$ , tends to slightly weaken its upper bound: for instance, the region allowed at 95% C.L. in the last panel of Fig. 10 is larger than the corresponding one in Fig. 7. In fact, the information coming from total rates prefers some energy dependence in the survival probability  $P_{ee}$ , and thus disfavors large values of  $\phi$  [see Eq. (2)]. However, since no clear indication for  $\partial P_{ee}/\partial E_\nu \neq 0$  emerges from the bulk of the SK spectrum, its addition in the fit makes large values of  $\phi$  slightly more “acceptable.” In addition, at  $\tan^2 \phi \gtrsim 1$ , the lower part of the broad region allowed by total rates (last three panels of Fig. 7) becomes more consistent with the (weak) indication for a nonzero night-day difference [Eq. (2)], thus giving some extra allowance for large values of  $\phi$ , as shown in the last three panels of Fig. 10.

Figure 11 is analogous to Fig. 10, the only difference being the flux of *hep* neutrinos (increased by a factor of 20 with respect to BP98). Since a large *hep* flux allows a better fit to the SK spectrum endpoint at any value of  $\phi$ , the global fit is somewhat improved (third

row of Tab. III), and the MSW solutions are slightly more extended than in Fig. 10. As for the  $2\nu$  case, the best-fit point migrates from the SMA to the LMA solution. In general, the comparison of Figs. 10 and 11 shows that the (uncertain) value of the *hep* neutrino flux is not crucial in shaping the current  $3\nu$  MSW solutions (although it might become decisive with more accurate spectral data).

Figure 12 shows the values of  $\chi^2 - \chi_{\min}^2$  as a function of  $\tan^2 \phi$  for unconstrained  $\delta m^2$  and  $\omega$ , coming from the fit to total rates and to all data. The values of  $\chi_{\min}^2$  can be read from Tab. III. This figure displays more clearly some anticipated features of the current  $3\nu$  MSW solutions (for standard *hep* flux): 1) a slight preference for nonzero values of  $\tan^2 \phi$ ; 2) the existence of an upper bound on  $\phi$ , slightly stronger in the fit to total rates ( $\phi \lesssim 55^\circ$  at 95% C.L.) than in the global fit ( $\phi \lesssim 58^\circ$ ). In the case of enhanced ( $20\times$ ) *hep* flux we find that: 1) the absolute minimum of  $\chi^2$  is reached at  $\tan^2 \phi = 0$  within the LMA solution; 2) for fixed  $\phi \neq 0$ , the local minimum migrates to the SMA solution when  $\tan^2 \phi \gtrsim 0.05$ ; and 3) the 95% C.L. upper limit on  $\tan^2 \phi$  is slightly weakened to  $\sim 59^\circ$ .

The 95% C.L. upper bound on  $\phi$  coming from solar neutrino data alone ( $\phi \lesssim 55^\circ$ – $59^\circ$ ) is consistent with the one coming from atmospheric neutrino data alone ( $\phi \lesssim 45^\circ$ ) [40], as well as with the upper limit coming from the combination of CHOOZ and atmospheric data ( $\phi \lesssim 15^\circ$ ) [35,40]. This indication supports the possibility that solar, atmospheric, and CHOOZ data can be interpreted in a single three-flavor oscillation framework [5,40]. In this case, the CHOOZ constraints on  $\phi$  exclude a large part of the  $3\nu$  MSW parameter space (basically all but the first two panels in Figs. 7–10).

However, even small values of  $\phi$  can be interesting for solar  $\nu$  phenomenology, as anticipated in the comment to Eq. (3). Figure 13 shows, for instance, how the partial and global fits to neutrino event rates (Cl, Ga, and SK experiments) are modified when passing from  $\tan^2 \phi = 0$  to  $\tan^2 \phi = 0.06$ . Each of the three experiments, taken separately, allows  $\omega \leq \pi/4$ . In the combination, the LOW and LMA solutions “touch” the  $\omega = \pi/4$  line at  $\tan \phi = 0$ , while for nonzero  $\phi$  only the LOW solution remains consistent with  $\omega = \pi/4$  (and, to some extent, with  $\omega > \pi/4$ ). This fraction of the LOW solution, usually ignored in analyses using the  $\sin^2 2\omega$  variable, can be relevant for model building. In particular, there is currently great interest in models predicting exact or nearly bimaximal mixing, namely,  $(\omega, \psi, \phi) \simeq (\pi/4, \pi/4, 0)$  (see, e.g., [50,51] and refs. therein). Such models imply, for the neutrino mixing matrix  $U_{\alpha i}$ , that  $U_{e1}^2 \simeq U_{e2}^2$  and that  $U_{e3}^2 \simeq 0$ . Recent theoretical predictions for (small) nonzero values of  $U_{e3}^2$  are discussed, e.g., in [52].

Figure 14 shows the section of the volume allowed in the  $3\nu$  MSW parameter space, for  $\omega = \pi/4$  (maximal mixing), in the mass-mixing plane ( $\delta m^2, \sin^2 \phi$ ). All data are included in the fit (with standard *hep* flux). It can be seen that both the LMA and LOW solutions are consistent with maximal mixing (at 99% C.L.) for  $\sin^2 \phi \equiv U_{e3}^2 = 0$ . Morever, the consistency of the LOW solution with maximal mixing improves significantly for  $U_{e3}^2 \simeq 0.1$ , while the opposite happens for the LMA solution. This gives the possibility to obtain nearly bimaximal mixing ( $\omega = \psi = \pi/4$  with  $\phi$  small) within the LOW solution to the solar neutrino problem—an interesting possibility for models predicting large mixing angles.

## V. SUMMARY

We have performed a thorough analysis of the  $2\nu$  and  $3\nu$  MSW solutions of the solar neutrino problem, discussing the information coming from the total rates, as well as from the SK energy spectrum and day-night asymmetry. The global fit to the data puts an upper bound to the  $\theta_{13}$  mixing angle, consistent with atmospheric and reactor oscillation searches. A fraction of the MSW solutions extends at and beyond maximal  $(\nu_1, \nu_2)$  mixing ( $\theta_{12} \geq \pi/4$ ), especially for the so-called LOW solution. Therefore, a novel realization of (nearly) bimaximal mixing models appears possible.

## ACKNOWLEDGMENTS

G.L.F. and E.L. thank the organizers of the *TAUP '99* Workshop on Topics in Astroparticle and Underground Physics (Paris, College de France), where preliminary results of this work were presented. E.L. thanks E. Kh. Akhmedov and P. I. Krastev for useful correspondence. This work is co-financed by the Italian Ministero dell'Università e della Ricerca Scientifica e Tecnologica (MURST) within the “Astroparticle Physics” project.

## APPENDIX: STATISTICAL ANALYSIS

In this appendix we present an updated version of the  $\chi^2$  statistical analysis of neutrino event rates discussed in Ref. [42], which has been widely used in many other analyses of the solar neutrino problem, including the one performed by the Super-Kamiokande Collaboration in [8]. In particular, we take into account the most recent estimates for the relevant BP98 standard solar model ingredients and for their uncertainties [23]. Unless otherwise noted, the notation is the same as in Ref. [42], to which the reader is referred for further details.

Table IV reports the solar neutrino fluxes  $\phi_i$ , as calculated in the BP98 Standard Solar Model [23]. The corresponding energy-averaged interaction cross sections  $C_{ij}$  for the  $j$ -th detector are given in Tab. V, taking into account updated energy spectra [23,24] and cross sections [24,26,25]. The associated  $1\sigma$  relative uncertainties  $\Delta \ln C_{ij}$  are reported in Tab. VI. Such tables allow the calculation of the theoretical uncertainties related to the detection process.

The uncertainties of the SSM  $\nu$  fluxes are mainly related on eleven basic ingredients  $X_k$ : five astrophysical  $S$ -factors, the Sun luminosity, the metallicity  $Z/X$ , the Sun age, the opacity, the element diffusion, and the  ${}^7\text{Be}$  electron capture rate  $C_{\text{Be}}$ . The last two sources of uncertainties represent new entries with respect to the list given in [42]. The “diffusion error” is estimated by taking differences between quantities calculated with and without diffusion [23]. The uncertainty in the  ${}^7\text{Be}(e^-, \nu_e){}^7\text{Li}$  capture rate [53] affects (inversely) the  ${}^8\text{B}$  flux by changing the  ${}^7\text{Be}$  density for the (much slower) competing reaction  ${}^7\text{Be}(p, \gamma){}^8\text{B}$ . The fractional  $1\sigma$  uncertainties of the eleven input ingredients ( $\Delta \ln X_k$ ) are reported in Tab. VII.

Table VIII reports the matrix  $\alpha_{ik}$  of logarithmic derivatives  $\partial \ln \phi_i / \partial \ln X_k$ , which parameterize the SSM “response” to small variations in the input ingredients, and which are

crucial to estimate correctly the correlations among the neutrino flux or event rate uncertainties [42]. As remarked in [42] for the opacity uncertainty, we have split the known flux errors  $\Delta \ln \phi_i = \alpha_{ik} \Delta \ln X_k$  due to opacity, diffusion, and  $^7\text{Be}$  electron capture, into two arbitrary factors,  $\alpha_{ik}$  and  $\Delta \ln X_k$  ( $k = 9, 10, 11$ ), so as to treat homogeneously all sources of uncertainties in the  $\chi^2$  statistics.

Given the previous ingredients, the standard event rates  $R_j$  are calculated as:

$$R_j = \sum_i R_{ij} = \sum_i \phi_i C_{ij} , \quad (\text{A1})$$

and the associated theoretical error matrix  $\sigma_{j_1 j_2}^2$  reads:

$$\sigma_{j_1 j_2}^2 = \delta_{j_1 j_2} \sum_i R_{ij_1}^2 (\Delta C_{ij_1})^2 + \sum_{i_1, i_2} R_{i_1 j_1} R_{i_2 j_2} \sum_k \alpha_{i_1 k} \alpha_{i_2 k} (\Delta \ln X_k)^2 . \quad (\text{A2})$$

The off-diagonal entries of  $\sigma_{j_1 j_2}^2$  induce strong correlations among the theoretical uncertainties for different experiments, as evident in Fig. 1. In the presence of oscillations (Figs. 3–5), the standard values of the partial rates  $R_{ij}$  are simply replaced by the corresponding oscillated values.

We remind that the entries of the  $\alpha_{ik}$  matrix are not independent, being constrained by the luminosity sum rule [42]. At equilibrium, the standard neutrino fluxes must obey the energy conservation relation [1]:

$$\sum_i (Q/2 - E_i) \phi_i = K , \quad (\text{A3})$$

where  $E_i$  is the average neutrino energy for the  $i$ -th neutrino flux,  $K = 0.853 \times 10^{12}$  MeV cm $^{-2}$  s $^{-1}$  is the solar luminosity, and  $Q = 26.73$  MeV is the overall  $Q$ -value for the fusion reaction  $4p \rightarrow \alpha + 2\nu_e + 2e^+$  (independent from the intermediate reaction chain).

Non-equilibrium corrections, which are especially relevant for CNO fluxes, modify this relation into [54,55]

$$\sum_i \xi_i \phi_i = K , \quad (\text{A4})$$

where the  $\xi_i$  values are given in Tab. IX. By taking partial derivatives of the above relation with respect to the input ingredients  $X_k$ , one gets the sum rule [42]:

$$\frac{\sum_i \xi_i \phi_i \alpha_{ik}}{\sum_i \xi_i \phi_i} = \delta_{k6} , \quad (\text{A5})$$

which is satisfied with good approximation ( $\sim 2\%$  level).

Similarly, if the flux variations are approximately parametrized as power laws of the central central temperature  $T$  of the Sun,

$$\phi_i(T) = \phi_i(T_0) \left( \frac{T}{T_0} \right)^{\beta_i} , \quad (\text{A6})$$

the temperature exponents  $\beta_i$  become constrained by the sum rule [42,54]

$$\frac{\sum_i \xi_i \beta_i \phi_i}{\sum_i \xi_i \phi_i} = 0 \quad (\text{A7})$$

which, using the exponents in Ref. [54], is satisfied only at the  $\sim 10\%$  level. However, such exponents can be easily adjusted within their uncertainties ( $\beta_i \rightarrow \tilde{\beta}_i$ ) so as to satisfy exactly the above sum rule. Sets of temperature exponents are given in Tab. X. The set of  $\tilde{\beta}_i$ 's is particularly relevant for analyses of the solar neutrino problem with “unconstrained” central temperature (not performed in this work).

Since the above tables and equations refer only to the analysis of the *total* neutrino event rates, a final remark is in order about the fit to the SK energy-angle spectral information. For MSW analyses, the maximum amount of information about the SK solar neutrino signal is contained in the double-differential distribution of events in nadir angle ( $\eta$ ) and electron recoil energy ( $E_e$ ). However, the  $(\eta, E_e)$  distribution is not yet available outside the SK collaboration, which has released only the two *projected* distributions, namely, the (angle-averaged) energy spectrum and the (energy-averaged) nadir distribution. The experimental errors of such projections (including statistical fluctuations) are *a priori* strongly correlated, but the published information is not sufficient to recover such correlations. For such reasons, while we include the complete information in  $E_e$  above 5.5 MeV (given as an 18-bin spectrum in [2,12,13]), we prefer to use only a minimal (but relevant) information in  $\eta$ , namely, the night-day asymmetry  $(N - D)/(N + D)$ .

The  $\chi^2$  function for the energy spectrum is then constructed in the same way as in Ref. [17], namely, by separating uncorrelated and correlated error components in the  $18 \times 18$  error matrix, with off-diagonal correlations equal to +1. A numerical table of errors is explicitly reported in [17] for the 825 day SK spectrum. Double counting of the total rate information in SK is avoided by minimizing the  $\chi^2$  with respect to the overall spectrum normalization, taken as a free parameter [17]. In the global fit, we then sum up the  $\chi^2$  of the spectrum, the  $\chi^2$  of the total rates, and the (trivial)  $\chi^2$  of the day-night asymmetry measurement. A similar construction of the global  $\chi^2$  function is also adopted in [18].

## TABLES

TABLE I. Solar neutrino event rates observed in the five experiments Homestake, Kamiokande, SAGE, GALLEX, and Super-Kamiokande (825 days,  $E_e > 6.5$  MeV), as compared with the theoretical expectations from the BP'98 standard solar model [23]. The quoted uncertainties are at  $1\sigma$ . In our analysis, the GALLEX and SAGE experimental rates are combined in quadrature in a single (Gallium) rate of  $72.5 \pm 5.6$  SNU.

Experiment	Experimental rate	Theoretical rate	Units	Ref.
Homestake	$2.56 \pm 0.16 \pm 0.16$	$7.7^{+1.2}_{-1.0}$	SNU	[19]
Kamiokande	$2.80 \pm 0.19 \pm 0.33$	$5.15^{+1.0}_{-0.7}$	$10^6 \text{ cm}^{-2} \text{ s}^{-1}$	[20]
SAGE	$67.2^{+7.2}_{-7.0} {}^{+3.5}_{-3.0}$	$129^{+8}_{-6}$	SNU	[21]
GALLEX	$77.5 \pm 6.2 {}^{+4.3}_{-4.7}$	$129^{+8}_{-6}$	SNU	[22]
Super-Kamiokande	$2.45 \pm 0.04 \pm 0.07$	$5.15^{+1.0}_{-0.7}$	$10^6 \text{ cm}^{-2} \text{ s}^{-1}$	[12]

TABLE II.  $2\nu$  MSW analysis: Absolute  $\chi^2$  values in selected points of the parameter space ( $\delta m^2, \sin^2 2\omega / \cos 2\omega$ ), corresponding to local  $\chi^2$  minima (SMA, LMA, LOW solutions) and to the no-oscillation case. Upper three rows: fit to total rates only (Cl+Ga+K+SK data). Middle three rows: fit to total rates (4 data), day-night asymmetry (1 datum), and SK energy spectrum (18 data with one adjustable normalization parameter). Lower three rows: as for the middle rows, but with *hep* flux increased by a factor 20. The number of degrees of freedom  $N_{\text{DF}}$  is equal to the number of data (either 4 or  $4 + 1 + 18 - 1$ ) minus 2 (the oscillation parameters). The last column corresponds to the probability of having a worse  $\chi^2$  fit *a priori*.

Observables	Solution	$\delta m^2$ (eV $^2$ )	$\sin^2 2\omega / \cos 2\omega$	$\chi^2$	$P(\chi^2, N_{\text{DF}})$
Rates only ( $N_{\text{DF}} = 2$ )	SMA	$5.89 \times 10^{-6}$	$5.62 \times 10^{-3}$	1.08	58.3 %
	LMA	$1.91 \times 10^{-5}$	1.62	4.59	10.1 %
	LOW	$1.07 \times 10^{-7}$	3.48	8.24	1.6 %
	no osc.	0	0	60.1	$9 \times 10^{-14}$
Rates, $N - D/N + D$ , spectrum ( $N_{\text{DF}} = 20$ )	SMA	$5.37 \times 10^{-6}$	$6.50 \times 10^{-3}$	27.3	12.7 %
	LMA	$2.55 \times 10^{-5}$	1.62	27.8	11.4 %
	LOW	$1.07 \times 10^{-7}$	2.87	30.8	5.8 %
	no osc.	0	0	85.8	$4 \times 10^{-10}$
Rates, $N - D/N + D$ , spectrum [ <i>hep</i> $\times 20$ ] ( $N_{\text{DF}} = 20$ )	SMA	$5.20 \times 10^{-6}$	$6.20 \times 10^{-3}$	25.6	17.9 %
	LMA	$2.94 \times 10^{-5}$	1.96	24.6	21.7 %
	LOW	$1.24 \times 10^{-7}$	2.87	27.8	11.4 %
	no osc.	0	0	71.9	$9 \times 10^{-8}$

TABLE III.  $3\nu$  MSW analysis: Absolute minima of the function  $\chi^2(\delta m^2, \tan^2 \omega, \tan^2 \phi)$  and their associated probability  $P$ . The number of degrees of freedom is  $N_{\text{DF}} = 1$  for the fit to total rates only and  $N_{\text{DF}} = 19$  for the global fit.

Observables	$\delta m^2$ (eV $^2$ )	$\tan^2 \omega$	$\tan^2 \phi$	$\chi^2_{\text{min}}$	$P(\chi^2, N_{\text{DF}})$
Rates only	$9.8 \times 10^{-6}$	$8.1 \times 10^{-4}$	0.1	0.70	40.3 %
All data	$9.8 \times 10^{-6}$	$7.1 \times 10^{-4}$	0.1	27.0	10.5 %
All data [ <i>hep</i> × 20]	$2.8 \times 10^{-5}$	0.37	0	24.5	17.8 %

TABLE IV. Neutrino fluxes  $\phi_i$  (cm $^{-2}$  s $^{-1}$ ) from the BP98 SSM [23].

pp × 10 $^{10}$	pep × 10 $^8$	hep × 10 $^3$	Be × 10 $^9$	B × 10 $^6$	N × 10 $^8$	O × 10 $^8$	F × 10 $^6$
5.94	1.39	2.10	4.80	5.15	6.05	5.32	6.33

TABLE V. Energy-averaged cross sections  $C_{ij}$ . Units are such that the expected partial rates  $R_{ij} = C_{ij}\phi_i$  are directly given in SNU for the Ga and Cl experiments, and as a ratio to the total BP98 predicted rate for Super-Kamiokande ( $E_e > 6.5$  MeV) and Kamiokande.

	pp × 10 $^{-9}$	pep × 10 $^{-8}$	hep × 10 $^{-6}$	Be × 10 $^{-9}$	B × 10 $^{-6}$	N × 10 $^{-9}$	O × 10 $^{-8}$	F × 10 $^{-8}$
Ga	1.17	2.04	7.14	7.17	2.40	6.04	1.14	1.14
Cl	0	0.16	4.26	0.24	1.14	0.17	0.07	0.07
K	0	0	0.595	0	0.194	0	0	0
SK	0	0	0.514	0	0.194	0	0	0

TABLE VI.  $1\sigma$  relative errors  $\Delta \ln C_{ij}$  of the energy averaged cross sections. The uncertainties of the (radiatively corrected)  $\nu$ -e scattering cross section in K and SK are negligible.

	pp	pep	hep	Be	B	N	O	F
Ga	0.023	0.170	0.320	0.070	0.320	0.060	0.120	0.120
Cl	0	0.020	0.037	0.020	0.032	0.020	0.020	0.020
K, SK	0	0	0	0	0	0	0	0

TABLE VII.  $1\sigma$  relative errors  $\Delta \ln X_k$  of the relevant SSM input parameters.

$S_{11}$	$S_{33}$	$S_{34}$	$S_{1,14}$	$S_{17}$	Lum	$Z/X$	Age	Opa	Diff	$C_{\text{Be}}$
0.017	0.060	0.094	0.143	0.106	0.004	0.033	0.004	0.02	0.02	0.02

TABLE VIII. Logarithmic derivatives  $\alpha_{ik} = \partial \ln \phi_i / \partial \ln X_k$ , parameterizing the response of neutrino fluxes  $\phi_i$  to variations in the SSM input parameters  $X_k$ .

	pp	pep	hep	Be	B	N	O	F
$S_{11}$	+0.14	-0.17	-0.08	-0.97	-2.59	-2.53	-2.93	-2.94
$S_{33}$	+0.03	+0.05	-0.45	-0.43	-0.40	+0.02	+0.02	+0.02
$S_{34}$	-0.06	-0.09	-0.08	+0.86	+0.81	-0.05	-0.05	-0.05
$S_{1,14}$	-0.02	-0.02	-0.01	+0.00	+0.01	+0.85	+1.00	+0.01
$S_{17}$	+0.00	+0.00	+0.00	+0.00	+1.00	+0.00	+0.00	+0.00
Lum	+0.73	+0.87	+0.12	+3.40	+6.76	+5.16	+5.94	+6.25
$Z/X$	-0.08	-0.17	-0.22	+0.58	+1.27	+1.86	+2.03	+2.09
Age	-0.07	+0.00	-0.11	+0.69	+1.28	+1.01	+1.27	+1.29
Opa	+0.14	+0.24	+0.54	-1.38	-2.62	-1.67	-2.05	-2.13
Diff	+0.13	+0.22	+0.13	-0.90	-2.00	-2.56	-2.75	-2.75
$C_{\text{Be}}$	+0.00	+0.00	+0.00	+0.00	-1.00	+0.00	+0.00	+0.00

TABLE IX. Neutrino energy parameters (in MeV) relevant for the luminosity sum rules [Eqs. (A3–A5)].

	pp	pep	hep	Be	B	N	O	F
$E_i$	0.261	1.442	9.625	0.813	6.735	0.706	0.994	1.000
$Q/2 - E_i$	13.10	11.92	3.74	12.55	6.63	12.66	12.37	12.37
$\xi_i$	13.10	11.92	10.17	12.55	6.63	3.457	21.57	2.36

TABLE X. Temperature exponents  $\beta_i$  and their  $\pm 1\sigma$  errors (from [54,1]). The exponents  $\tilde{\beta}_i$  represent our best-fit adjustments, which satisfy exactly the luminosity sum rule [Eq. (A7)].

	pp	pep	hep	Be	B	N	O	F
$\beta_i$	$-1.1 \pm 0.1$	$-2.4 \pm 0.9$	$4.5 \pm 1.5$	$10 \pm 2$	$24 \pm 5$	$24.4 \pm 0.2$	$27.1 \pm 0.1$	$27.8 \pm 0.1$
$\tilde{\beta}_i$	-1.1039	-2.407	4.5	8.79	23.996	24.4	27.099	27.8

## REFERENCES

- [1] J. N. Bahcall, *Neutrino Astrophysics* (Cambridge University Press, Cambridge, England, 1989).
- [2] Y. Totsuka, in *PANIC'99*, XVth Particles And Nuclei International Conference (Uppsala, Sweden, 1999), to appear; Report available at <http://www-sk.icrr.u-tokyo.ac.jp/doc/sk/pub>
- [3] G. L. Fogli, E. Lisi, and D. Montanino, Phys. Rev. D **49**, 3626 (1994); Astropart. Phys. **4**, 177 (1995).
- [4] T. K. Kuo and J. Pantaleone, Rev. Mod. Phys. **61**, 937 (1989).
- [5] G. L. Fogli, E. Lisi, and D. Montanino, Phys. Rev. D **54**, 2048 (1996).
- [6] L. Wolfenstein, Phys. Rev. D **17**, 2369 (1978); S. P. Mikheyev and A. Yu. Smirnov, Yad. Fiz. **42**, 1441 (1985) [Sov. J. Nucl. Phys. **42**, 913 (1985)]; Nuovo Cim. C **9** (1986), 17.
- [7] Super-Kamiokande Collaboration, Y. Fukuda *et al.*, Phys. Rev. Lett. **82**, 2430 (1999).
- [8] Super-Kamiokande Collaboration, Y. Fukuda *et al.*, Phys. Rev. Lett. **82**, 1810 (1999).
- [9] R. Barbieri, L. J. Hall, D. Smith, A. Strumia, and N. Weiner, J. High Energy Phys. **12**, 017 (1998).
- [10] T. Teshima, T. Sakai, and O. Inagaki, Int. J. Mod. Phys. A **14**, 1953 (1999).
- [11] J. S. Kim and C. W. Kim, hep-ph/9909428.
- [12] Y. Suzuki for the Super-Kamiokande Collaboration, in *Lepton-Photon '99*, Proceedings of the XIX International Symposium on Photon and Lepton Interactions at High Energies (Stanford, California, U.S.A., 1999), to appear; transparencies available at <http://lp99.slac.stanford.edu>
- [13] M. Nakahata in *TAUP '99*, VIth International Workshop on Topics in Astroparticle and Underground Physics (Paris, France, 1999), to appear; transparencies available at <http://taup99.in2p3.fr/TAUP99>
- [14] N. Hata and P. Langacker, Phys. Rev. D **56**, 6107 (1997).
- [15] G. L. Fogli, E. Lisi, and D. Montanino, Astropart. Phys. **9**, 119 (1998).
- [16] J. N. Bahcall, P. I. Krastev, and A. Yu. Smirnov, Phys. Rev. D **58**, 096016 (1998).
- [17] M. C. Gonzalez-Garcia, P. C. de Holanda, C. Peña-Garay, and J. W. F. Valle, hep-ph/9906469 (to appear in Nucl. Phys. B).
- [18] J. N. Bahcall, P. I. Krastev, and A. Yu. Smirnov, hep-ph/9911248
- [19] Homestake Collaboration, B. T. Cleveland, T. J. Daily, R. Davis Jr., J. R. Distel, K. Lande, C. K. Lee, P. S. Wildenhain, and J. Ullman, Astrophys. J. **496**, 505 (1998).
- [20] Kamiokande Collaboration, Y. Fukuda *et al.*, Phys. Rev. Lett. **77**, 1683 (1996).
- [21] SAGE Collaboration, J. N. Abdurashitov *et al.*, Phys. Rev. C **60**, 055801 (1999).
- [22] GALLEX Collaboration, W. Hampel *et al.*, Phys. Lett. B **447**, 127 (1999).
- [23] J. N. Bahcall, S. Basu and M. Pinsonneault, Phys. Lett. B **433**, 1 (1998); see also J. N. Bahcall's homepage, <http://www.sns.ias.edu/~jnb>
- [24] J. N. Bahcall, E. Lisi, D. E. Alburger, L. DeBraeckeleer, S. J. Freedman, and J. Napoli-tano, Phys. Rev. C **54**, 411 (1996).
- [25] J. N. Bahcall, M. Kamionkowski, and A. Sirlin, Phys. Rev. D **51**, 6146 (1995).
- [26] J. N. Bahcall, Phys. Rev. C **56**, 3391 (1997).
- [27] E. Lisi and D. Montanino, Phys. Rev. D **56**, 1792 (1997).
- [28] V. A. Kuzmin, Phys. Lett. **17**, 27 (1965).

- [29] J. N. Bahcall, J. M. Gelb, and S. P. Rosen, Phys. Rev. D **35**, 2979 (1987); J. N. Bahcall and W. C. Haxton, Phys. Rev. D **40**, 931 (1989).
- [30] R. Escribano, J. M. Frère, A. Gevaert, and D. Monderen, Phys. Lett. B **444**, 397 (1998); J. N. Bahcall and P. I. Krastev, Phys. Lett. B **436**, 243 (1998).
- [31] G. Fiorentini, V. Berezinsky, S. Degl'Innocenti, and B. Ricci, Phys. Lett. B **444**, 387 (1998).
- [32] C. J. Horowitz, Phys. Rev. C **60**, 022801 (1999).
- [33] A. H. Guth, L. Randall, and M. Serna, J. High Energy Phys. **8**, 018 (1999).
- [34] A. de Gouvea, A. Friedland, and H. Murayama, hep-ph/9910286
- [35] G. L. Fogli, in *TAUP '99* [13].
- [36] C. Giunti, Phys. Rev. D **59**, 077301 (1999).
- [37] S. M. Bilenky, C. Giunti, and C. W. Kim, Phys. Lett. B **380**, 331 (1996).
- [38] P. F. Harrison, D. H. Perkins, W. G. Scott, Phys. Lett. B **374**, 111 (1996).
- [39] CHOOZ Collaboration, M. Apollonio *et al.*, Phys. Lett. B **420**, 397 (1998); hep-ex/9907037
- [40] G. L. Fogli, E. Lisi, A. Marrone, and G. Scioscia, Phys. Rev. D **59**, 033001 (1999).
- [41] B. Faïd, G. L. Fogli, E. Lisi, and D. Montanino, Astropart. Phys. **10**, 93 (1999).
- [42] G. L. Fogli and E. Lisi, Astropart. Phys. **3**, 185 (1995).
- [43] The Review of Particle Physics, C. Caso *et al.*, Europ. Phys. Journal C **3**, 1 (1998).  
See the review on Probability (for hypotheses tests) and on Statistics (for parameter estimation).
- [44] The SNO Collaboration, J. Boger *et al.*, nucl-ex/9910016 (submitted to Nucl. Instrum. and Methods).
- [45] F. Villante, G. Fiorentini, and E. Lisi, Phys. Rev. D **59**, 013006 (1999).
- [46] T. A. Kirsten, in *Neutrino '98*, Proceedings of the XVIII International Conference on Neutrino Physics and Astrophysics (Takayama, Japan, 1998), edited by Y. Suzuki and Y. Totsuka; Nucl. Phys. B (Proc. Suppl.) **77** (1999), p. 26.
- [47] G. L. Fogli, E. Lisi, D. Montanino, and A. Palazzo, hep-ph/9910387
- [48] L. Oberauer, in *Neutrino '98*, [46], p. 48.
- [49] A. Suzuki, *Neutrino '98*, [46], p. 171.
- [50] G. Altarelli and F. Feruglio, Phys. Lett. B **439**, 112 (1998); J. High Energy Phys. **11**, 021 (1998).
- [51] A. Yu. Smirnov, in *Moriond '99*, Proceedings of the XXXIV Rencontres de Moriond: Electroweak Interactions and Unified Theories (Les Arcs, France, 1999), to appear; hep-ph/9907296
- [52] E. Kh. Akhmedov, G. C. Branco, and M. N. Rebelo, hep-ph/9912205
- [53] A. V. Gruzinov and J. N. Bahcall, Astrophys. J. **490**, 437 (1997).
- [54] J. N. Bahcall and A. Ulmer, Phys. Rev. D **53**, 4202 (1996).
- [55] J. N. Bahcall and P. I. Krastev, Phys. Rev. D **53**, 4211 (1996).

## FIGURES

FIG. 1. The solar neutrino deficit, shown as a discrepancy between data and expectations in the gallium (Ga), chlorine (Cl), and Super-Kamiokande total event rates. In each plane, the error ellipses represent 99% C.L. contours for two degrees of freedom (i.e.,  $\Delta\chi^2 = 9.21$ ). The projection of an ellipse onto one of the axis gives approximately the  $\pm 3\sigma$  range for the corresponding rate. Data and expectations refer to Table I. The correlation of SSM errors is calculated as in the Appendix.

FIG. 2. Two-generation MSW solutions to the solar neutrino problem. The upper four panels correspond to the following separate fits to data subsets: total rates (Cl+Ga+K+SK); Super-Kamiokande night-day asymmetry  $N - D/N + D$ ; Super-Kamiokande electron energy spectrum with standard *hep* neutrino flux; Super-Kamiokande spectrum with enhanced ( $20\times$ ) *hep* neutrino flux. The two lower panels show the results of global fits to all data. The thin solid, thick solid, and dashed curves correspond to  $\chi^2 - \chi^2_{\min} = 4.61, 5.99$ , and  $9.21$ . The positions of the local  $\chi^2$  minima in fits including the total rates are indicated by dots. See also Tab. II.

FIG. 3. The SMA solution at best fit (total rates only, first row of Tab. II), compared with the experimental data, in the same planes as in Fig. 1. Note the excellent agreement between theory and observations.

FIG. 4. As in Fig. 3, but for the LMA solution at best fit (total rates only, second row of Tab. II).

FIG. 5. As in Fig. 3, but for the LOW solution at best fit (total rates only, third row of Tab. II).

FIG. 6. Comparison of data and predictions for the Super-Kamiokande spectrum shape. The theoretical spectra normalization is taken free in the fit. The upper (lower) panel corresponds to the case of standard ( $20\times$ ) *hep* flux. The SMA, LMA, and LOW spectra are calculated in the global best fit points reported in Tab. II (middle rows for the upper panel and lower rows for the lower panel). The SK data are reported from [2,12,13], and the error bars refer to statistical and total experimental errors.

FIG. 7. Three-flavor MSW oscillations: global fit to Cl+Ga+K+SK rates in the  $(\delta m^2, \tan^2 \omega, \tan^2 \phi)$  parameter space. The favored regions in each panel correspond to sections of the volume allowed at 90%, 95%, and 99% C.L. ( $\chi^2 - \chi^2_{\min} = 6.25, 7.82$ , and  $11.36$ ) for representative values of  $\tan^2 \phi$ .

FIG. 8. As in Fig. 7, but for the fit to the Super-Kamiokande night-day asymmetry. The region inside the curves is excluded.

FIG. 9. As in Fig. 7, but for the fit to the Super-Kamiokande energy spectrum. The regions inside the curves are excluded.

FIG. 10. Results of the global three-flavor MSW fit to all data. Notice that, in the first two panels, the 99% C.L. contours are compatible with maximal mixing ( $\tan^2 \omega = 1$ ) for both the LOW and the LMA solutions.

FIG. 11. As in Fig. 10, but for the case of enhanced ( $20\times$ ) *hep* flux. The allowed regions are slightly enlarged with respect to Fig. 10.

FIG. 12. Values of  $\Delta\chi^2$  as a function of  $\phi$ , for unconstrained  $\delta m^2$  and  $\tan^2 \omega$ . At 95% C.L., the upper limit on  $\phi$  is in the range  $55^\circ$ – $59^\circ$ , depending on the data used in the fit and on the value of the *hep* flux.

FIG. 13. Regions allowed at 99% C.L. by the total rates only, for  $\tan^2 \phi = 0$  (solid curves) and  $\tan^2 \phi = 0.06$  (dotted curves). For  $\tan^2 \phi = 0.06$ , the SMA and LMA solutions are slightly shifted to lower values of  $\tan^2 \omega$ , while the LOW solution is shifted to higher values (including the value  $\omega = \pi/4$ ).

FIG. 14. Section of the allowed volume in the  $3\nu$  parameter space in the plane  $(\delta m^2, \sin^2 \phi)$ , for the case of maximal  $(\nu_1, \nu_2)$  mixing ( $\omega = \pi/4$ ). For  $\sin^2 \phi = 0$ , both the LMA and LOW solutions are compatible with maximal mixing at 99% C.L. For small values of  $\sin^2 \phi$ , the maximal mixing case favors the LOW solution.

## Solar neutrino deficit, 1999

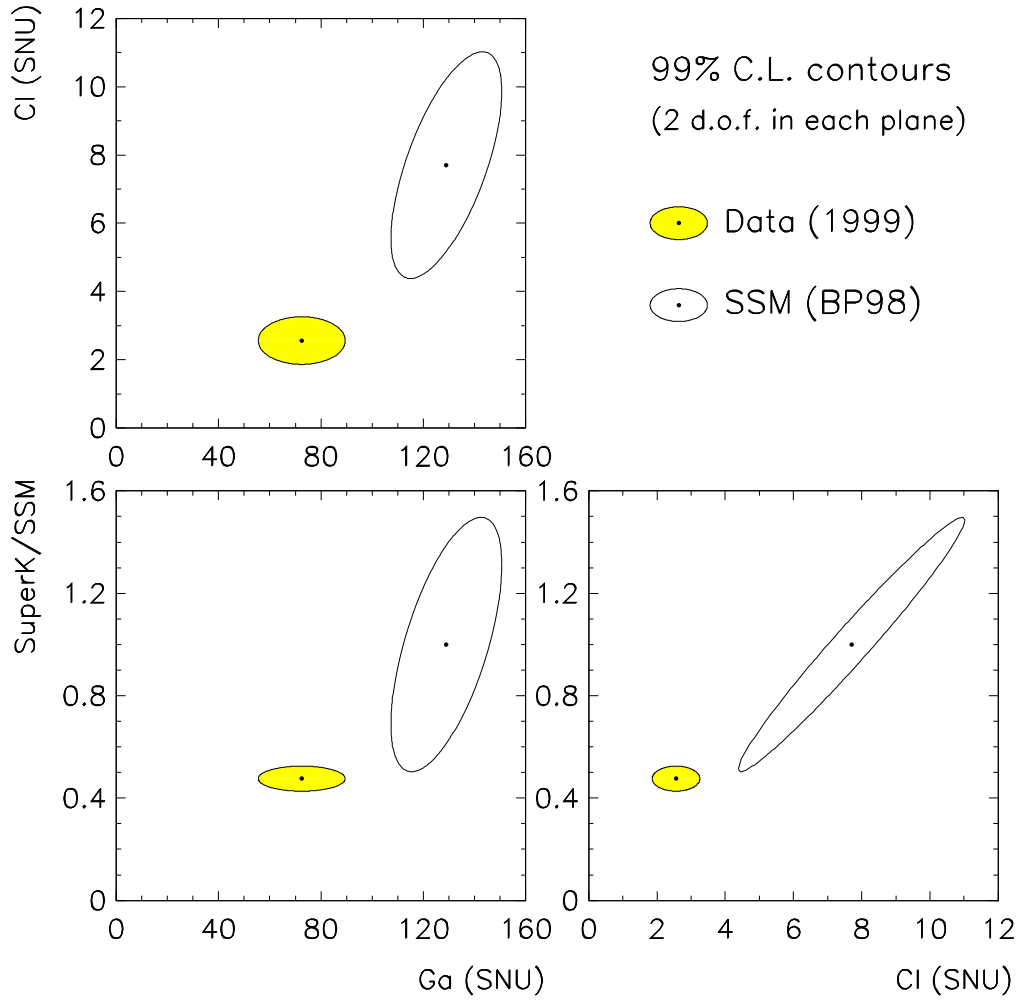


FIG. 1. The solar neutrino deficit, shown as a discrepancy between data and expectations in the gallium (Ga), chlorine (Cl), and Super-Kamiokande total event rates. In each plane, the error ellipses represent 99% C.L. contours for two degrees of freedom (i.e.,  $\Delta\chi^2 = 9.21$ ). The projection of an ellipse onto one of the axis gives approximately the  $\pm 3\sigma$  range for the corresponding rate. Data and expectations refer to Table I. The correlation of SSM errors is calculated as in the Appendix.

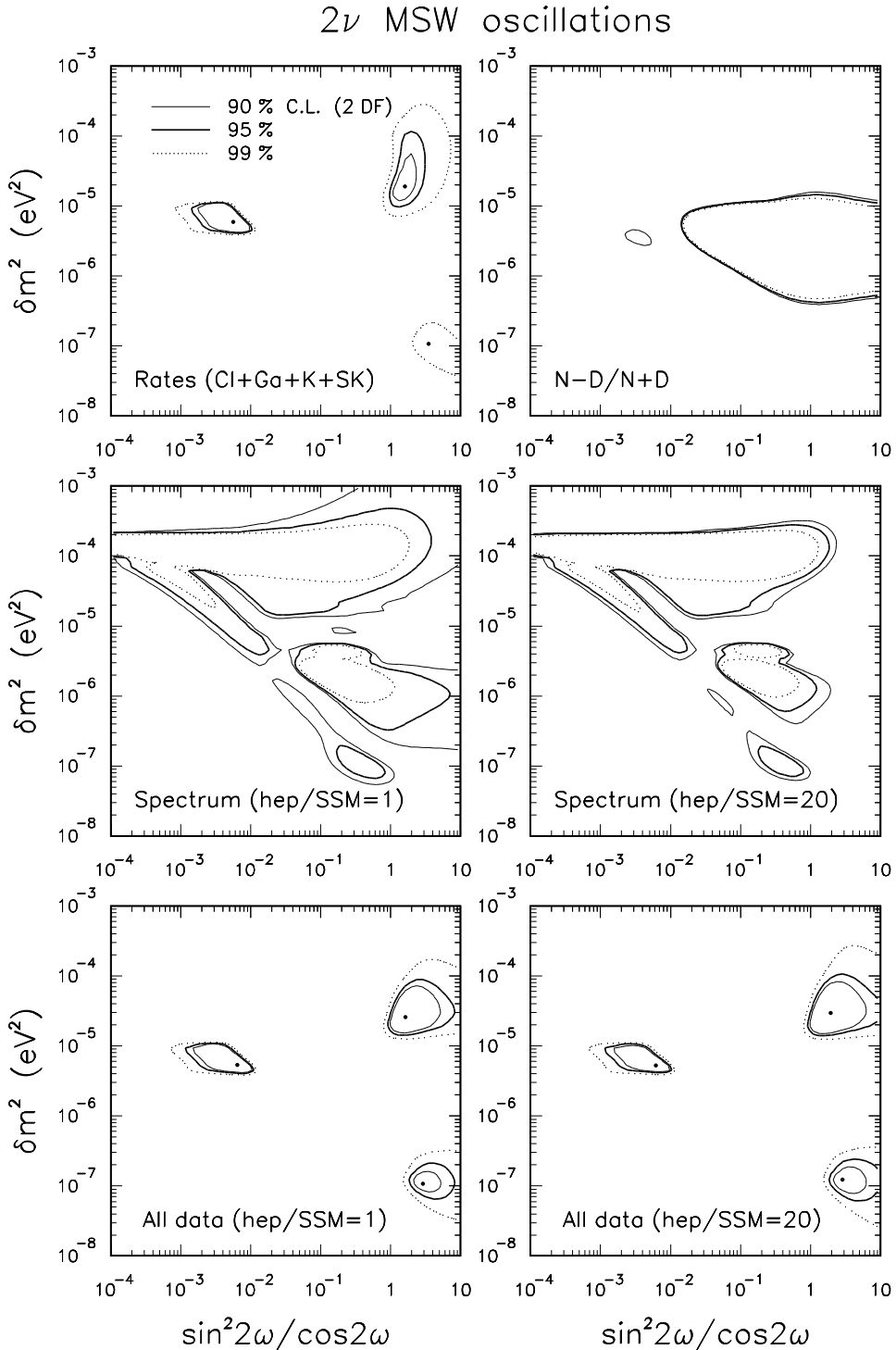


FIG. 2. Two-generation MSW solutions to the solar neutrino problem. The upper four panels correspond to the following separate fits to data subsets: total rates (Cl+Ga+K+SK); Super-Kamiokande night-day asymmetry  $N - D/N + D$ ; Super-Kamiokande electron energy spectrum with standard *hep* neutrino flux; Super-Kamiokande spectrum with enhanced ( $20\times$ ) *hep* neutrino flux. The two lower panels show the results of global fits to all data. The thin solid, thick solid, and dashed curves correspond to  $\chi^2 - \chi^2_{\min} = 4.61, 5.99$ , and  $9.21$ . The positions of the local  $\chi^2$  minima in fits including the total rates are indicated by dots. See also Tab. II.

## MSW oscillations, SMA solution

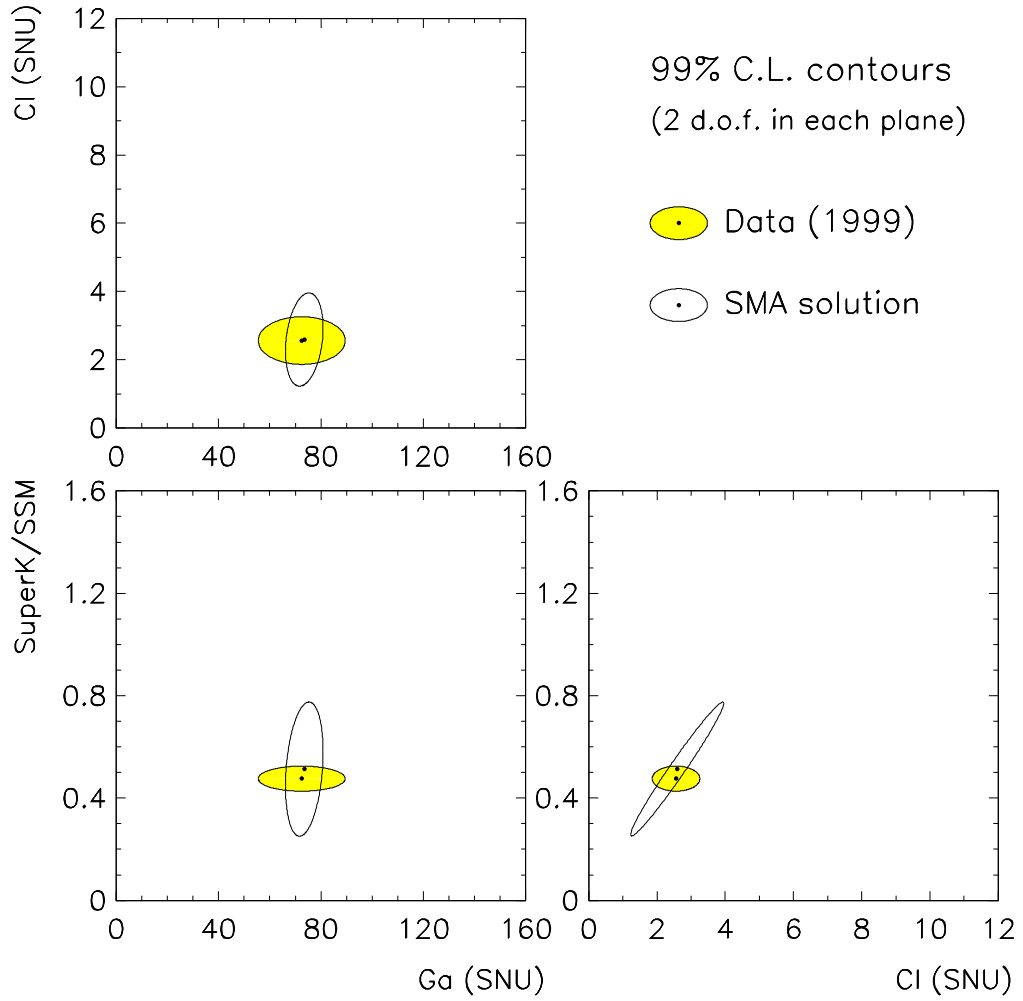


FIG. 3. The SMA solution at best fit (total rates only, first row of Tab. II), compared with the experimental data, in the same planes as in Fig. 1. Note the excellent agreement between theory and observations.

## MSW oscillations, LMA solution

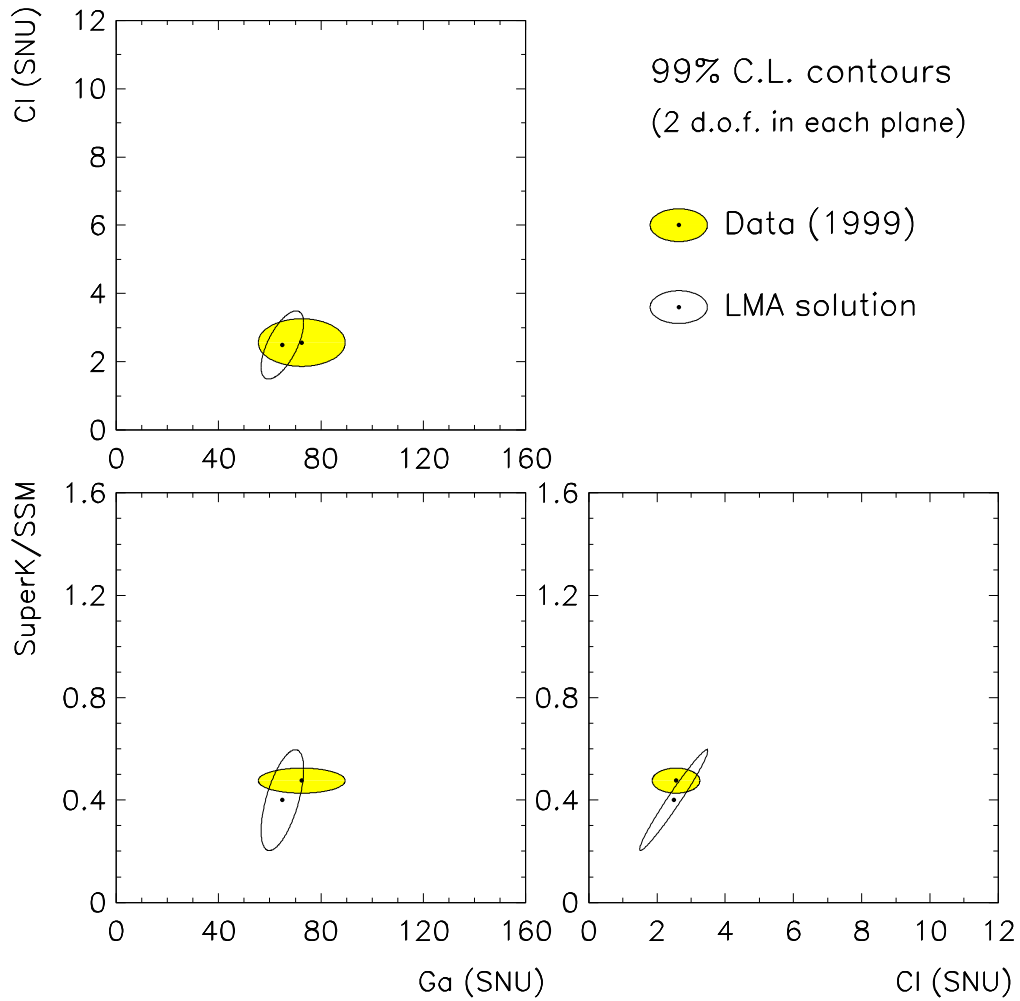


FIG. 4. As in Fig. 3, but for the LMA solution at best fit (total rates only, second row of Tab. II).

## MSW oscillations, LOW solution

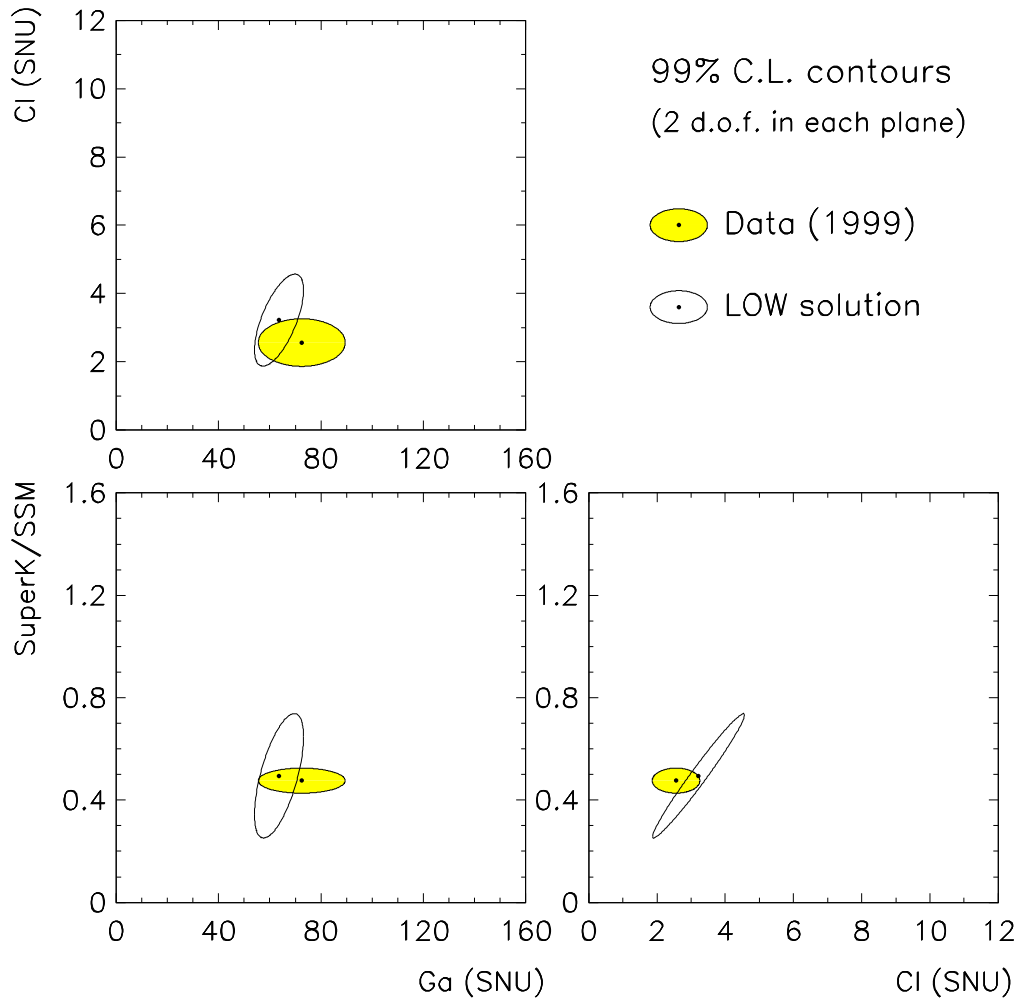


FIG. 5. As in Fig. 3, but for the LOW solution at best fit (total rates only, third row of Tab. II).

### Super-Kamiokande electron energy spectrum

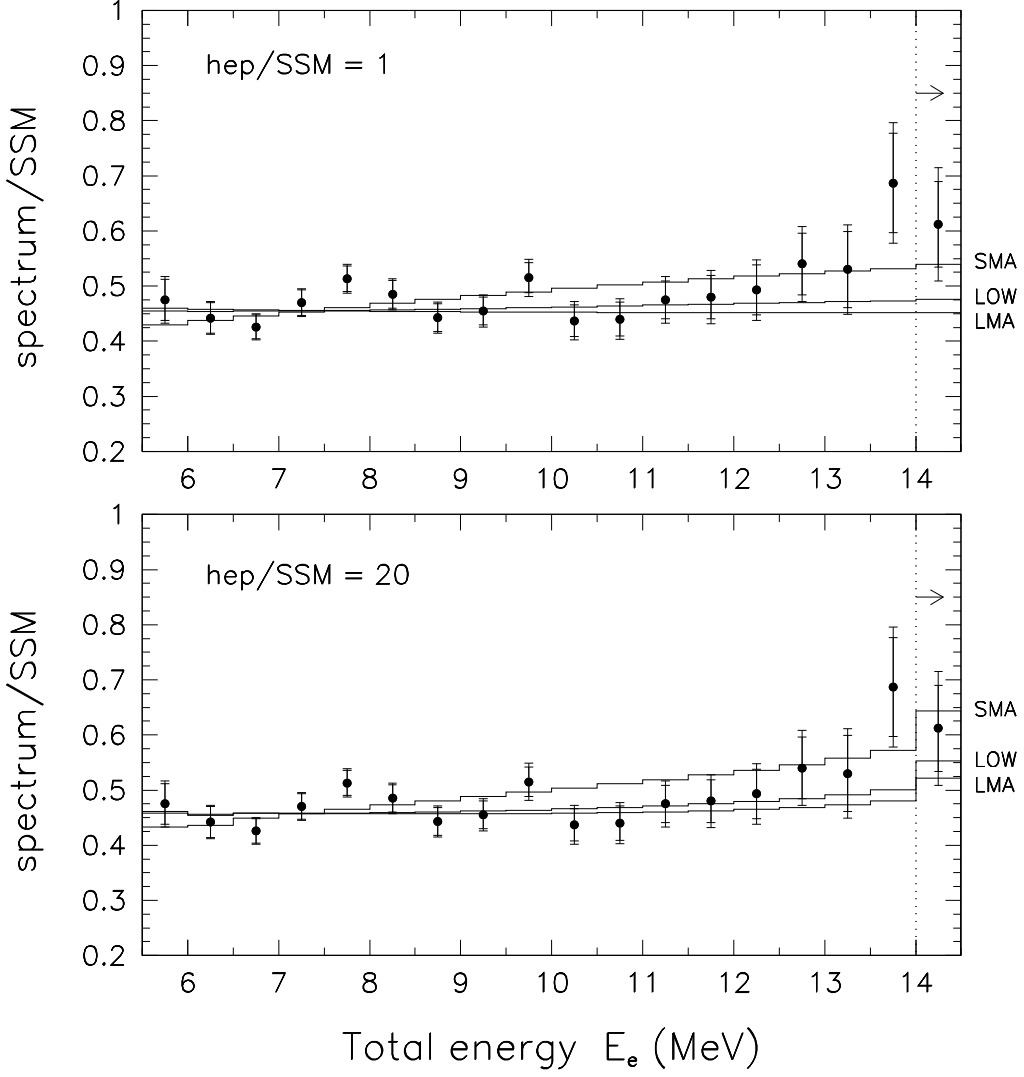


FIG. 6. Comparison of data and predictions for the Super-Kamiokande spectrum shape. The theoretical spectra normalization is taken free in the fit. The upper (lower) panel corresponds to the case of standard ( $20\times$ ) *hep* flux. The SMA, LMA, and LOW spectra are calculated in the global best fit points reported in Tab. II (middle rows for the upper panel and lower rows for the lower panel). The SK data are reported from [2,12,13], and the error bars refer to statistical and total experimental errors.

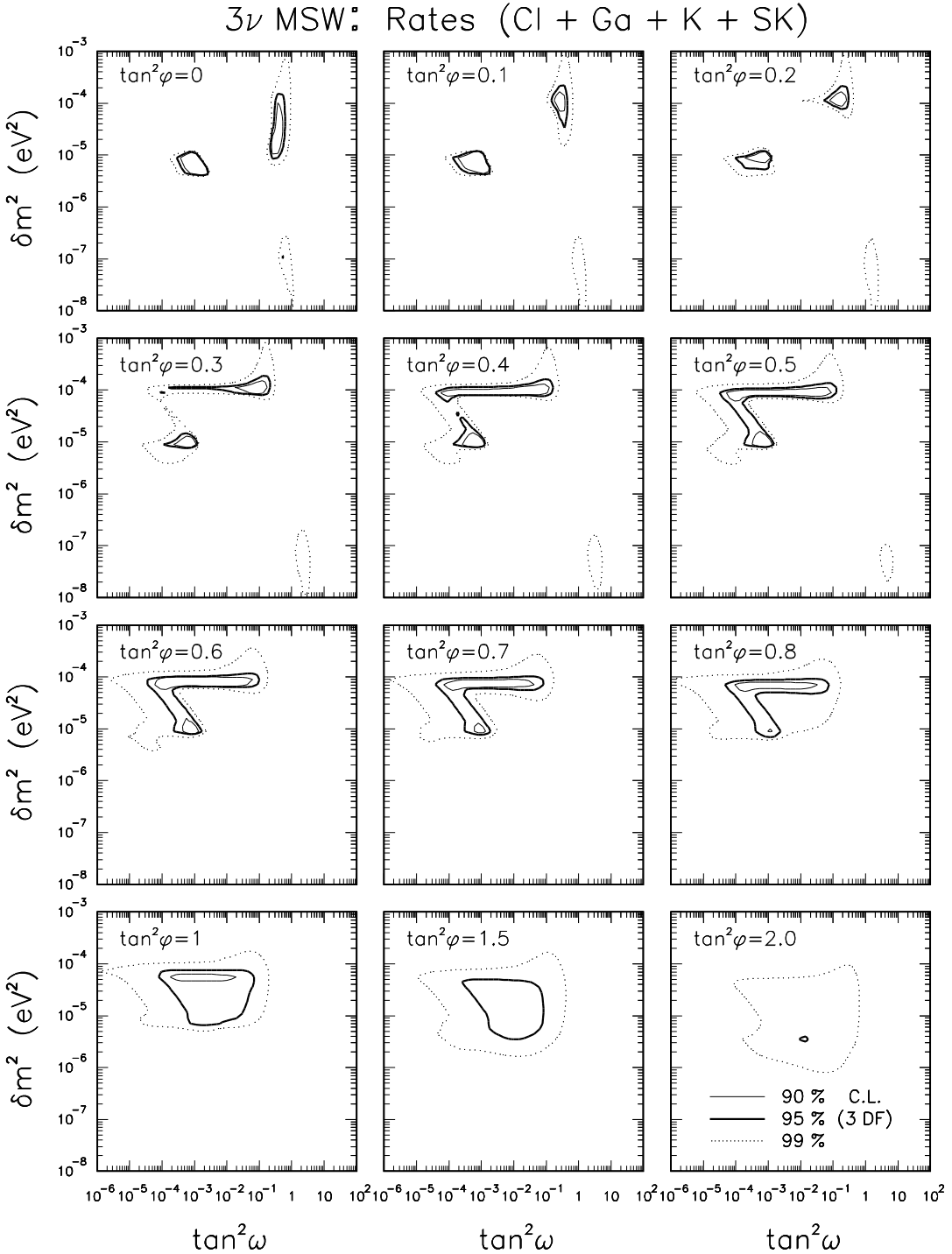


FIG. 7. Three-flavor MSW oscillations: global fit to Cl+Ga+K+SK rates in the  $(\delta m^2, \tan^2 \omega, \tan^2 \phi)$  parameter space. The favored regions in each panel correspond to sections of the volume allowed at 90%, 95%, and 99% C.L. ( $\chi^2 - \chi_{\min}^2 = 6.25, 7.82$ , and  $11.36$ ) for representative values of  $\tan^2 \phi$ .

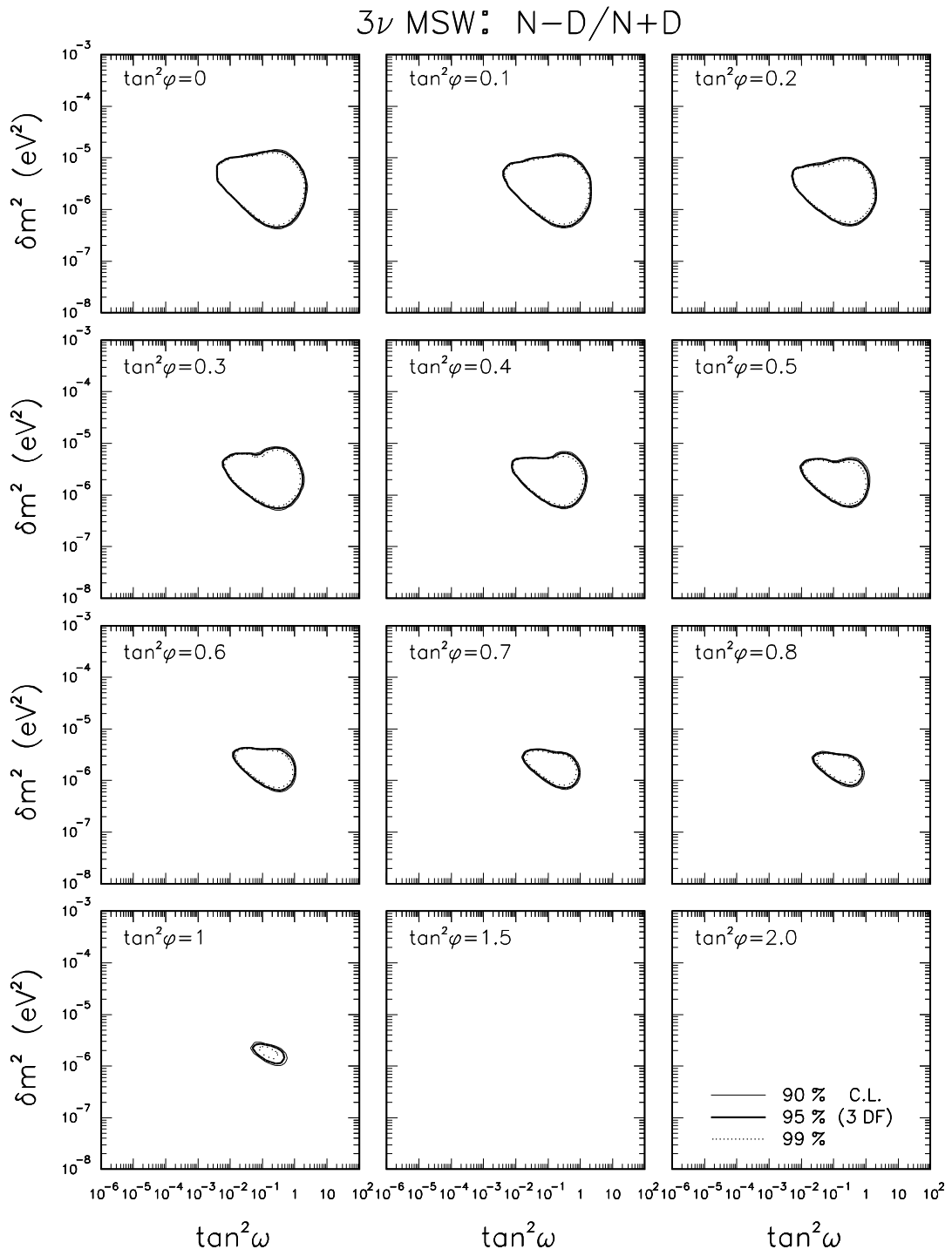


FIG. 8. As in Fig. 7, but for the fit to the Super-Kamiokande night-day asymmetry. The region inside the curves is excluded.

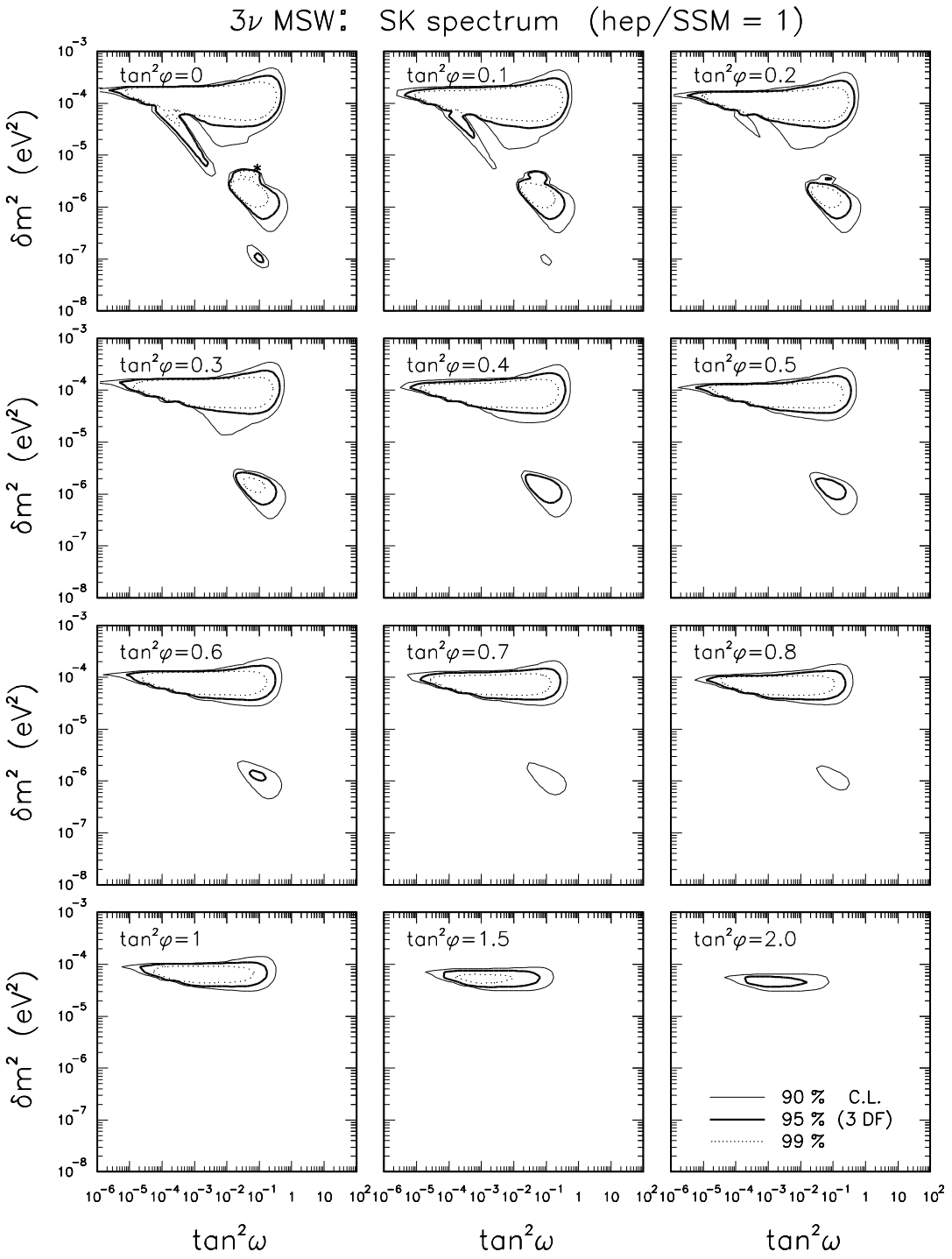


FIG. 9. As in Fig. 7, but for the fit to the Super-Kamiokande energy spectrum. The regions inside the curves are excluded.

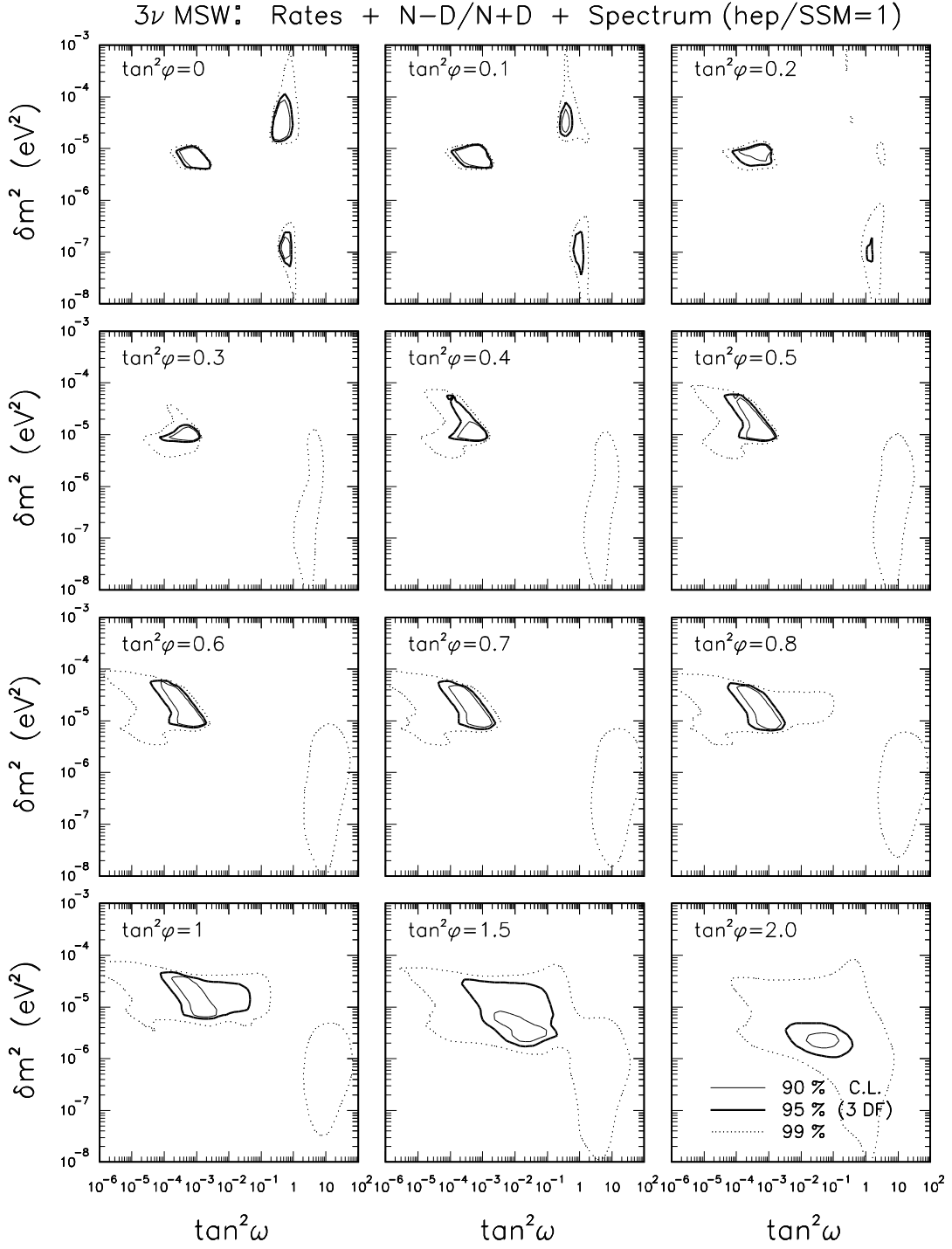


FIG. 10. Results of the global three-flavor MSW fit to all data. Notice that, in the first two panels, the 99% C.L. contours are compatible with maximal mixing ( $\tan^2 \omega = 1$ ) for both the LOW and the LMA solutions.

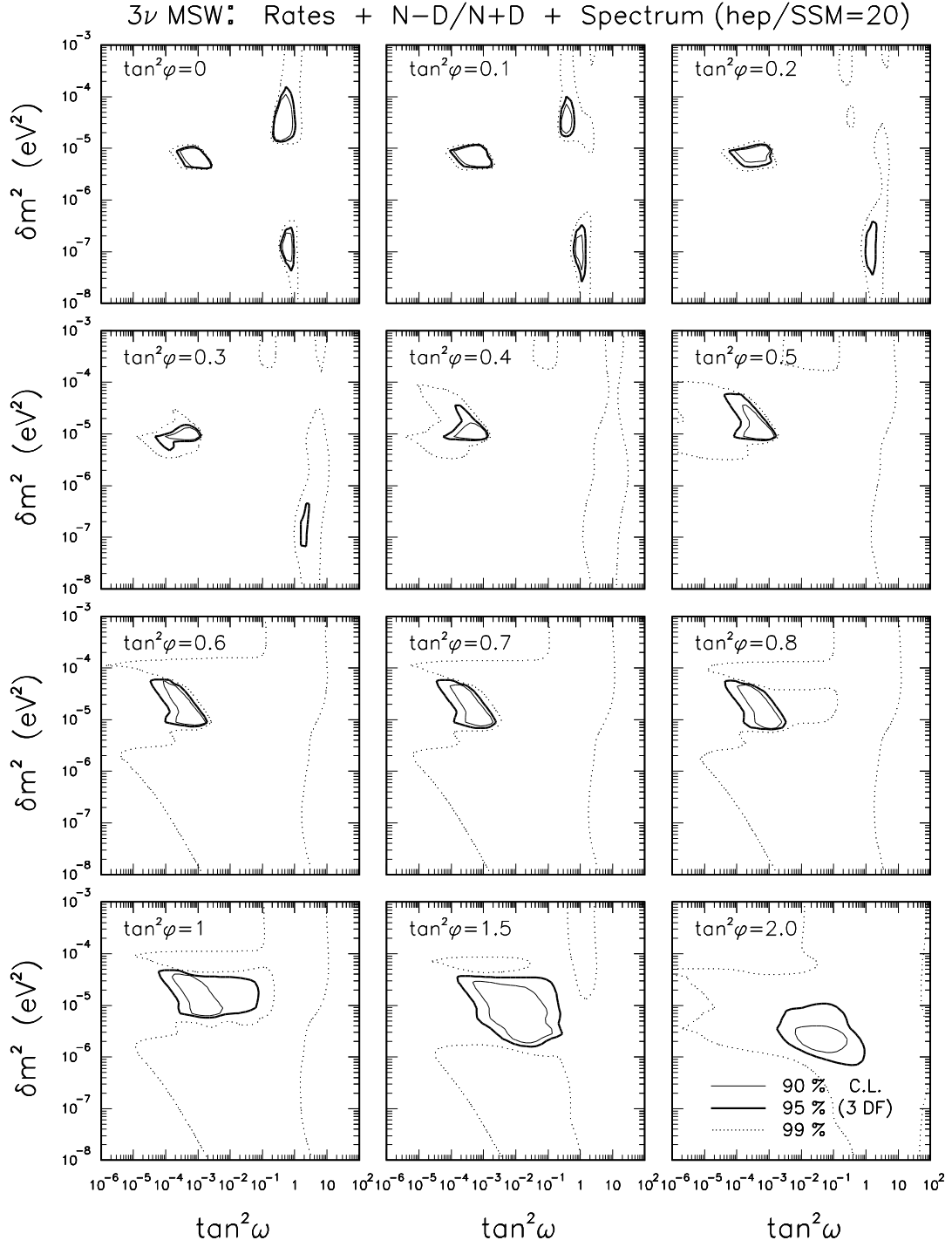


FIG. 11. As in Fig. 10, but for the case of enhanced (20 $\times$ ) *hep* flux. The allowed regions are slightly enlarged with respect to Fig. 10.

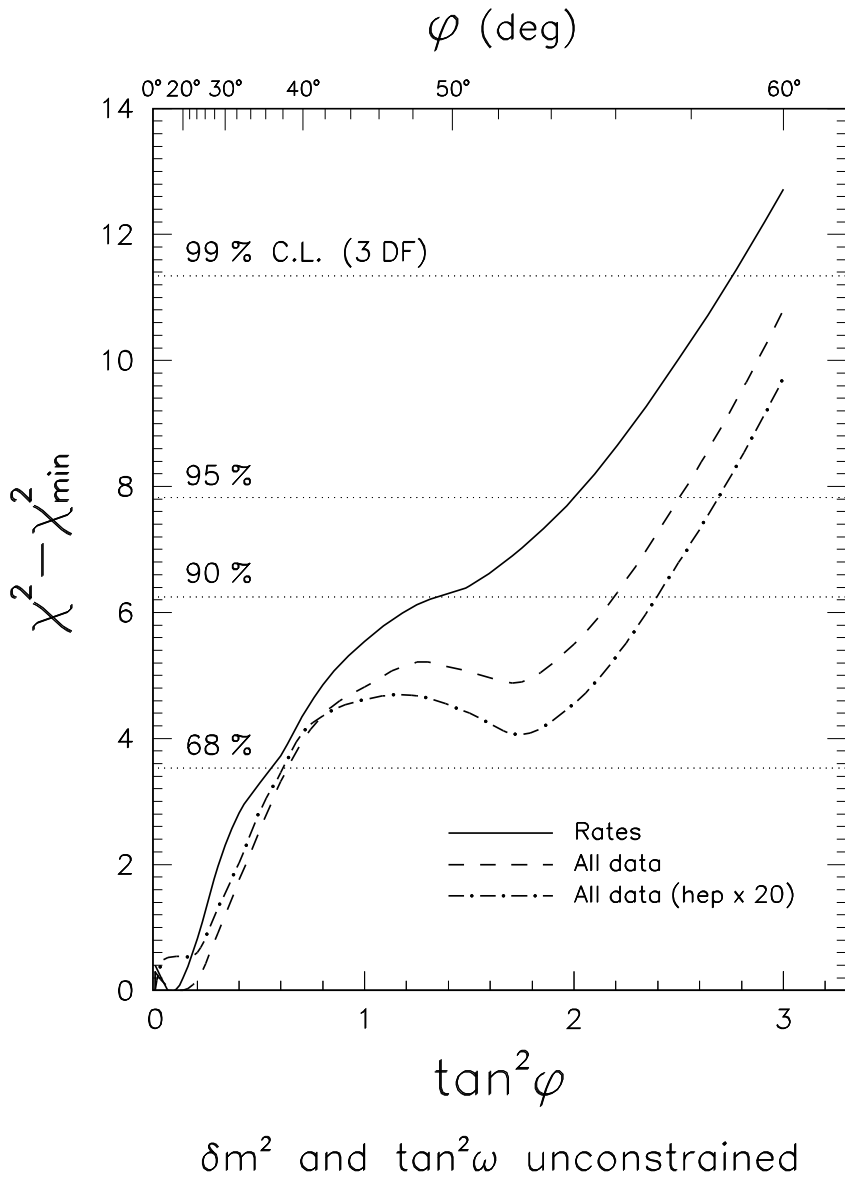


FIG. 12. Values of  $\Delta\chi^2$  as a function of  $\phi$ , for unconstrained  $\delta m^2$  and  $\tan^2 \omega$ . At 95% C.L., the upper limit on  $\phi$  is in the range  $55^\circ$ – $59^\circ$ , depending on the data used in the fit and on the value of the *hep* flux.

Regions allowed by rates (99% C.L., DF=3)

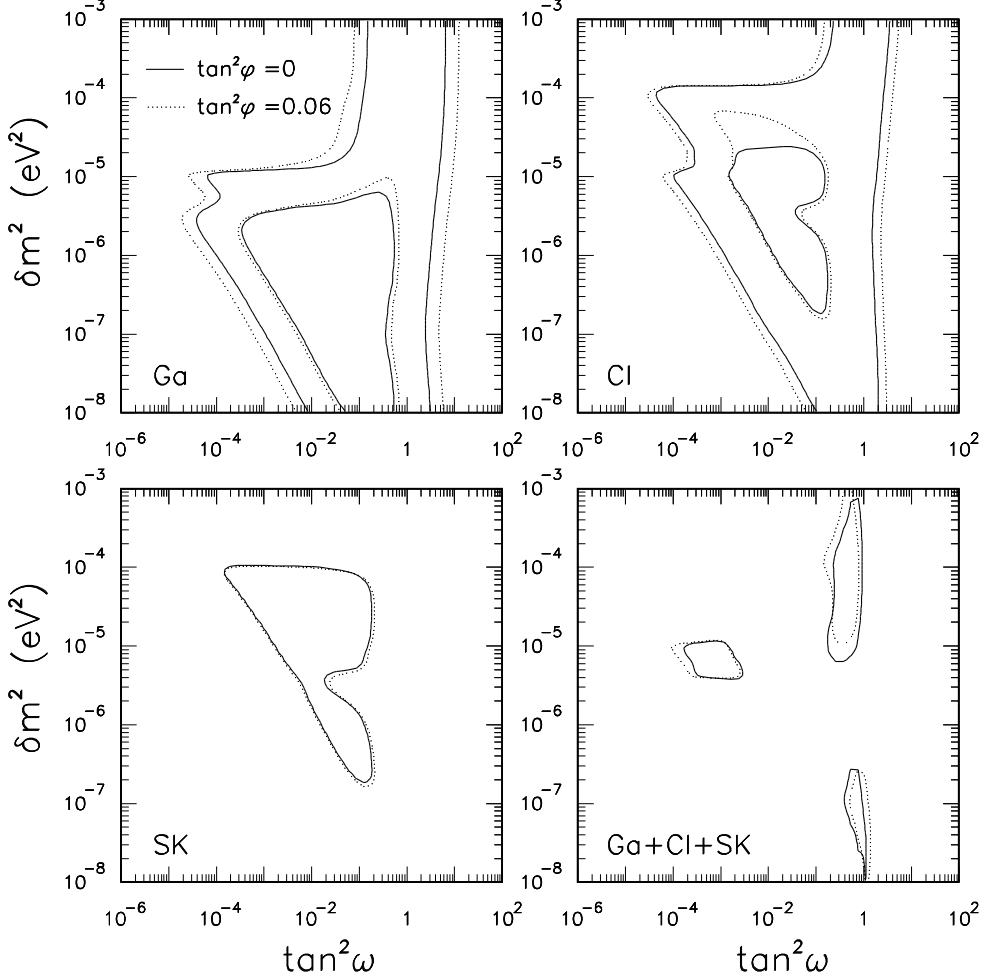


FIG. 13. Regions allowed at 99% C.L. by the total rates only, for  $\tan^2 \phi = 0$  (solid curves) and  $\tan^2 \phi = 0.06$  (dotted curves). For  $\tan^2 \phi = 0.06$ , the SMA and LMA solutions are slightly shifted to lower values of  $\tan^2 \omega$ , while the LOW solution is shifted to higher values (including the value  $\omega = \pi/4$ ).

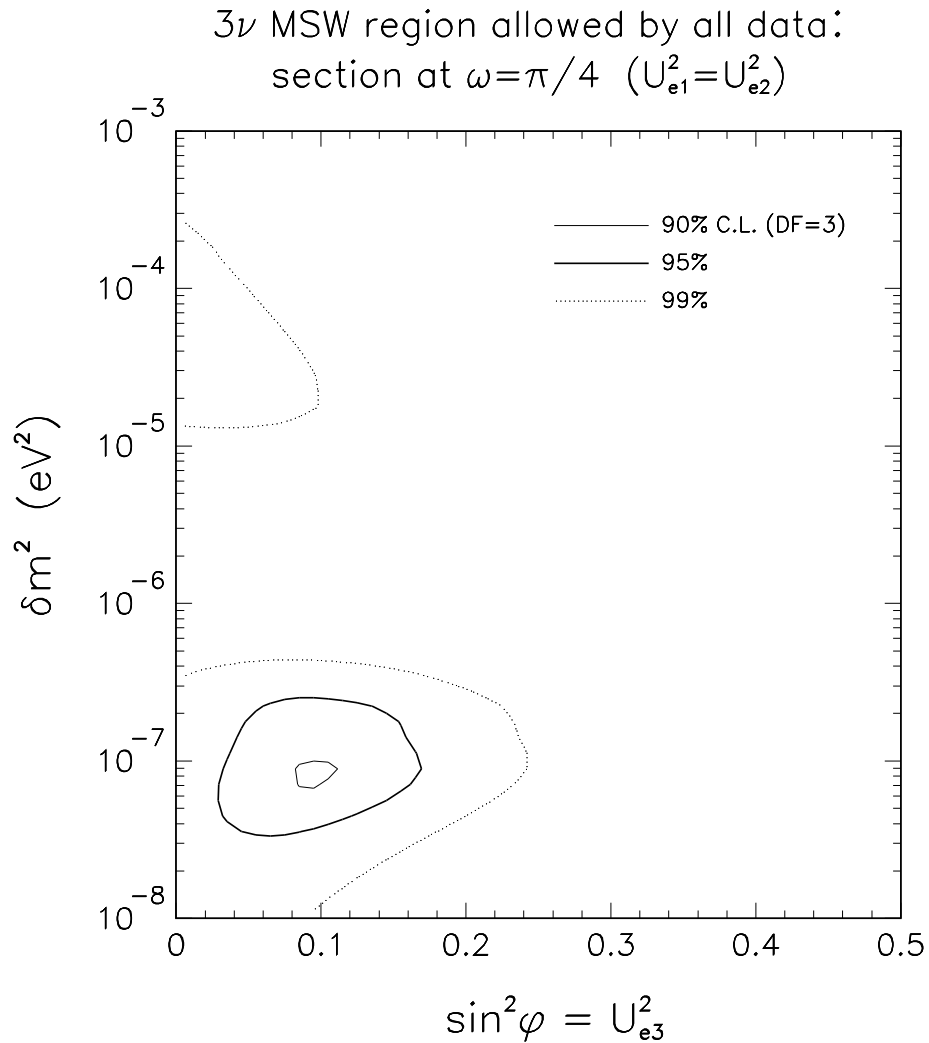


FIG. 14. Section of the allowed volume in the  $3\nu$  parameter space in the plane  $(\delta m^2, \sin^2 \phi)$ , for the case of maximal  $(\nu_1, \nu_2)$  mixing ( $\omega = \pi/4$ ). For  $\sin^2 \phi = 0$ , both the LMA and LOW solutions are compatible with maximal mixing at 99% C.L. For small values of  $\sin^2 \phi$ , the maximal mixing case favors the LOW solution.